Seismic reservoir characterization of potential CO_2 storage reservoir sandstones in Smeaheia area, Northern North Sea

Manzar Fawad [a,*], MD Jamilur Rahman [a], Nazmul Haque Mondol [a,b]

[a] *University of Oslo, Norway*
[b] *Norwegian Geotechnical Institute, Norway*

A B S T R A C T

Evaluating any subsurface CO_2 storage site comprises the reservoir, seal, and overburden investigation to mitigate injection and storage-related complications. The Upper-Middle Jurassic Sognefjord, Fensfjord, and Krossfjord formation sandstones are potential CO_2 storage reservoirs at the Smeaheia area, northern North Sea. The Smeaheia area is located east of the Troll oil and gas field. The Upper Jurassic organic-rich Heather and Draupne Formation shales are the main seals for the sandstone reservoirs. In this study, we carried out a prestack seismic inversion to obtain elastic property cubes of acoustic impedance (*AI*), velocity ratio (*Vp/Vs*), and bulk density (*RhoB*). From these elastic cubes, we obtained the reservoir properties such as porosity (*Phi*), shaliness (V_{sh}), and permeability (*k*) of Sognefjord, Fensfjord, and Krossfjord formations. We introduced two new equations to extract the shale volume and porosity cubes from the inverted elastic cubes in the present study. These equations are nonlinear based on the *AI* versus *Vp/Vs* rock physics template. Both equations are correlated first with the well log data and then applied on the elastic property cubes (*AI* versus *Vp/Vs*) to obtain the V_{sh} and *Phi* property cubes. An additional porosity cube (*PhiD*) was generated from the inverted *RhoB* for comparison. Finally, using an empirical equation, permeability was extracted from the porosity cube. The reservoir properties we derived from 3D seismic, in addition to the well log, revealed the vertical and lateral variations of porosity, shaliness, and permeability in the Smeaheia area. We used these reservoir properties to infer the depositional environment and the viability of reservoirs for CO_2 storage. The depositional environments identified were shoreface and deltaic from the extracted sand-body geometries. We found the Sognefjord Formation possessing the best reservoir properties, followed by the Fensfjord Formation as the secondary storage potential. In contrast, the Krossfjord Formation owed the lowest reservoir quality in the Smeaheia area.

1. Introduction

Subsurface CO_2 storage is one of the many solutions proposed for reducing greenhouse gas emissions in the atmosphere. A hydrocarbon trap is a demonstration of a working reservoir, seal, and overburden system; however, in a subsurface geological CO_2 sequestration, the storage and capping elements viability requires proper investigation. This study focuses on a prestack seismic inversion to obtain the reservoir properties (e.g., porosity, shaliness, and permeability) of Sognefjord, Fensfjord, and Krossfjord formations in a potential CO_2 storage site "Smeaheia" offshore Norway (Fig. 1a). The Smeaheia area is located east of the Troll field in the Bjørgvin Arch and Stord Basin in the northern North Sea. The area is bounded by an array of faults separating the Troll Field in the west by the Vette Fault (VF) and the Caledonian Basement

Complex in the east by the Øygarden Fault Complex (ØFC). There are two structural closures in the Smeaheia area 'Alpha-32/4-1' in the east and the 'Beta-32/2-1' in the west, possessing dry wells (Fig. 1b). The area is among the few potential CO_2 storage sites under consideration in the northern North Sea.

Fig. 2a shows a stratigraphic succession (Jurassic and younger rocks) at the exploration well 32/4-1 (Alpha prospect) in the Smeaheia area. The primary reservoir sandstone is the Sognefjord Formation, which consists of coastal-shallow marine sands, overlain by the Heather and Draupne Formation shales, the main caprocks in the area. The Sognefjord Formation is medium to coarse-grained, well-sorted, friable, locally micaceous, and minor argillaceous sandstone. The Fensfjord Formation is fine to medium-grained, well-sorted, and moderately friable to consolidated sandstones with shale intercalations. The
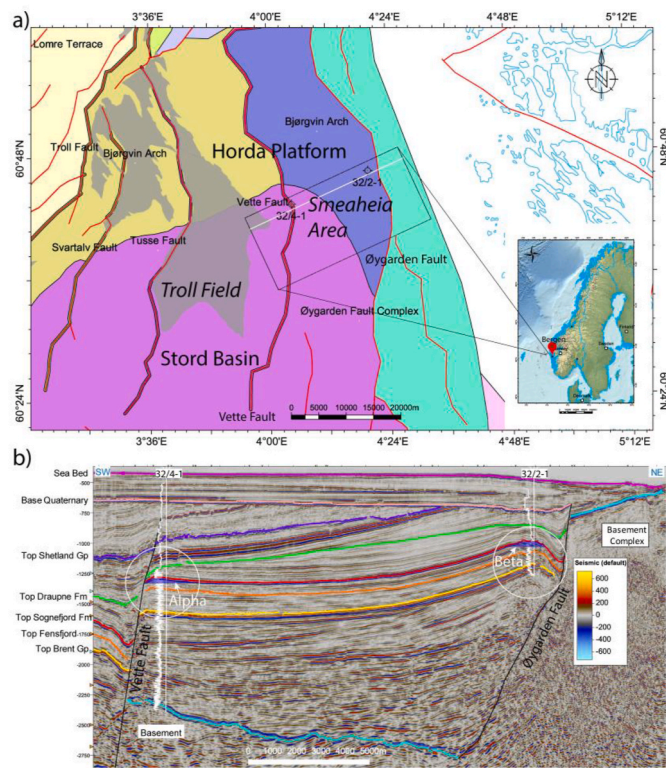

Fig. 1. (a) Location of the CO_2 storage site Smeaheia, offshore Norway. (b) A SW-NE running inline-1066 of 3D survey GN1101 over the Smeaheia area showing the Alpha and Beta prospects and other regional structures delineated by the key surfaces. Two dry wells are present in the area with trajectories highlighted on the seismic section by gamma-ray (GR) curves.

Fig. 2. (a) A generalized Jurassic to Quaternary stratigraphic succession in the study area (modified from Kinn et al., 1997). (b) A west to east stratigraphic cross-section between the wells 32/4-1 and 32/2-1 flattened on top Draupne Formation (primary seal). The potential reservoir sandstones of Sognefjord, Fensfjord, and Krossfjord formations show several prograding cycles.

Krossfjord Formation is medium to coarse-grained, well-sorted, and loose to friable sandstone. Bioclastic material and occasional cemented bands occur in all the three potential reservoir sandstones of Sognefjord, Fensfjord, and Krossfjord formations. The Heather Formation shale interfingers with sandstones of the Krossfjord, Fensfjord, and Sognefjord formations (Fig. 2b). It consists mainly of silty claystone with thin streaks of limestone, occasionally becoming highly micaceous grading into sandy siltstone (NPD, 2020). The Draupne Formation comprises dark grey-brown to black, usually non-calcareous, carbonaceous, and fissile claystones. It is characterized by high gamma-ray radioactivity (often above 100 API units) because of the elements associated with organic matter. The Draupne Formation deposited in a marine environment had restricted bottom circulation, mostly under anaerobic conditions (NPD, 2020). The Heather and Draupne Formations combined are the primary seals for the CO_2 storage reservoir sandstones of the Sognefjord and the underlying formations.

Considering only the Sognefjord Formation having good reservoir quality, a CO_2 storage reservoir, Alpha and Beta structures have a potential storage capacity of roughly 100 Mt each (Statoil, 2016). The main risks of leakage of injected CO_2 in the Smeaheia area are sideways migration along the ØFC and fractures towards the east, where the reservoir juxtaposes the fractured basement rocks and the VF in the west (Fig. 1b). Other risks are associated with numerous faults/fractures of sub-seismic resolution and fluid pathways related to palaeo- and sea-floor pockmarks (Mulrooney et al., 2018). The topmost layer (Fig. 2a, Quaternary sediments) of the overburden is glacial sediments comprising of claystone and till, and their thickness ranges from about 50 m and up to more than 200 m (Halland et al., 2014). There is also a concern of pressure communication with the Troll field that produces oil and gas from the same reservoir sandstones. The Troll field lies about 8 km west of the Smeaheia area on the VF hanging wall.
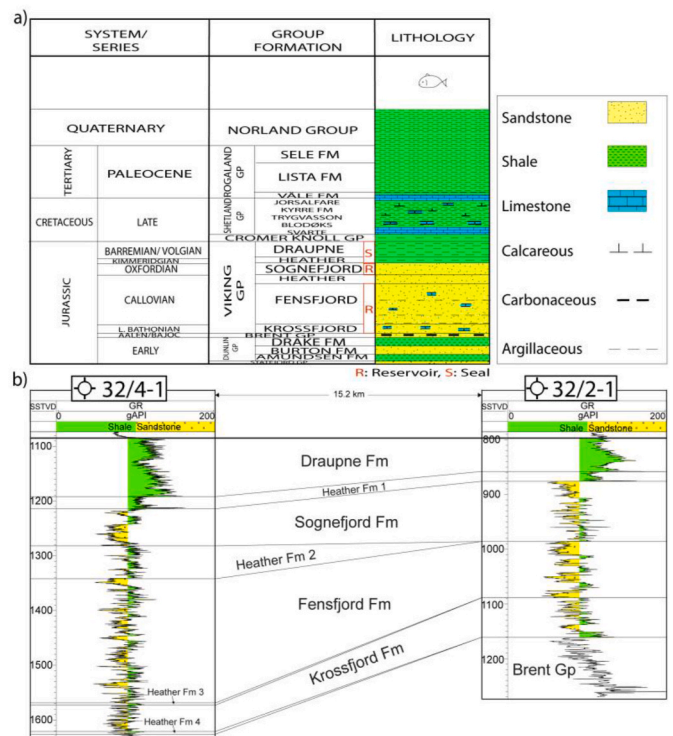
For evaluating a potential GCS, the storage and capping integrity are critical, which need proper investigation. The target Jurassic sandstones in the Smeaheia area from the well log data seem suitable for CO_2 geological storage for having the required physical properties, i.e., porosity, permeability, and water salinity. However, it is essential to know the subtle horizontal variations in addition to the vertical changes in reservoir properties (for instance, porosity and permeability) to predict the behavior of an injected CO_2 plume and its migration updip, or vertically upward to the base of the reservoir seal (Chadwick et al., 2004; Riley, 2010). A 3D reservoir simulation model constructed by stochastically distributing various properties from well log data cannot predict the CO_2 plume movement and associated risks. Therefore, it is crucial to extract reservoir properties using 3D seismic data volume to extend and complement the well log data.

A seismic profile is an array of processed seismic traces, with each trace being considered to be the convolution of a source wavelet with an input reflectivity sequence with each reflectivity spike representative of the contrast in acoustic impedance (AI = P- wave velocity x bulk density) across the geological contact. The magnitude of AI and other elastic parameters in a formation depends upon many factors such as rock mineralogy, texture, pore fluid type, saturation, effective pressure, and compaction level that provide the relationship between rock physics, litho-fluid facies, and depositional environments (Avseth et al., 2005; Chuhan et al., 2003; Fawad et al, 2010, 2011; Giles, 1997; Hart et al., 2013; Mondol et al., 2008a; Schmitt, 2015; Thyberg et al., 2000). The mineralogy and texture depend upon the depositional environments, whereas the degree of compaction is a function of the depth of burial and temperature (Bjørkum et al., 1998). The compaction trend of both shale and sand behave differently with the depth influencing the seismic signatures (Brown, 2010; Fawad et al., 2010; Mondol et al., 2007). The properties of rocks gradually change from the time of deposition, through burial at the greater depth and convert the loose sands to

sandstones (Bernabé et al., 1992; Bjørlykke and Egeberg, 1993), and the soft clay particles into brittle mudstones (Aplin and Macquaker, 2011; Thyberg et al., 2009). The main diagenetic processes are stress-dependent mechanical compaction (MC) and temperature plus time-dependent chemical compaction (CC), which converts the reservoir and caprock properties into the present state (Bjørlykke and Jahren, 2015).

Extracting reservoir properties and fluid detection from seismic has always been an objective of geophysicists since active source reflection seismic has been used for hydrocarbon exploration (Fawad et al., 2020; Sheriff and Geldart, 1995). Standard reservoir characterization workflows comprise seismic inversion and amplitude-variation-with-offset (AVO) or amplitude-variation-with-angle (AVA) analyses. The change in amplitude with angle has long been developed by Zoeppritz in 1919 (Zoeppritz, 1919). Since the Zoeppritz equations were not intuitive, many approximations to solve AVO/AVA have been presented over the years (e.g., Aki and Richards, 1980; Fatti et al., 1994; Goodway et al., 1997; Shuey, 1985; Smith and Gidlow, 1987; Verm and Hilterman, 1995).

The *AI,* which is a real physical material property, is a zero-offset reflection function. On the contrary, an elastic impedance (*EI*) is not a physical property but a derived attribute of the seismic data, which can be computed for non-normal incident angles (Connolly, 1999). The *EI* contains fluid information. The *EI* method is further improved by Whitcombe et al. (2002), calling it Extended Elastic Impedance (*EEI*) with the option of a theoretical rotation angle (*chi*) from $-90°$ to $+90°$ in the intercept-gradient crossplot space. Particular rotation angles are related to elastic parameters, such as Lambda-Mu-Rho (*LMR*) (Goodway et al., 1997) and the compressional-to-shear wave velocity ratio (*Vp/Vs*). The *LMR* parameters are useful lithology and fluid discriminators.

Seismic inversion is a well-established technique since 1972 when Lindseth (1972) put forward a new method of processing, displaying, and interpreting seismic data that was mainly the inverse of producing seismograms from borehole sonic logs. The basic procedure uses the reflectivity at an interface between two successive layers to derive the layers' effective elastic properties. At present various types of seismic inversion algorithms exist, e.g., colored impedance inversion (Lancaster and Whitcombe, 2000), simultaneous AVO inversion (Hampson et al., 2005; Ma, 2001), and joint facies-based impedance inversion (Kemper and Gunning, 2014). The inversion may utilize either post-stack or prestack seismic data, employing deterministic or stochastic procedures, with or without a background low-frequency model.

Geostatistical methods consider the uncertainties of spatial correlation, conditioning to different kinds of data, and incorporating sub seismic heterogeneities (Bosch et al., 2010; Buland and Omre, 2003; Zhao et al., 2014). The stochastic inversion methods using a general Bayesian formulation are implemented in two different workflows (Bosch et al., 2010). In the sequential approach, first seismic data are inverted, deterministically or stochastically, into elastic properties. The inversion-derived elastic properties are then converted to the rock properties using a rock physics model (Dvorkin and Nur, 1996; Ødegaard and Avseth, 2004). The joint or simultaneous workflow accounts for the elastic parameters and the reservoir properties, often in a Bayesian formulation, assuring stability between the elastic and reservoir properties. Rock physics models link elastic parameters such as impedances and velocities to the reservoir properties such as lithologies, porosity, and fluids. Generally, the inversion is based on ray-tracing modeling on a single interface assumption, which introduces errors and requires substantial pre-processing for stratified models. To overcome those problems, a joint PP and PS Pre-stack Seismic Inversion for Stratified Models Based on the Propagator Matrix Forward Engine has been proposed (Luo et al., 2020). The authors demonstrated the algorithm to be better than the single PP inversion in terms of consistency and accuracy, especially for S-wave velocity and density.

In terms of layer properties, the *EEI* represents a straight line rotation in a crossplot of *AI* versus *Vp/Vs* (Avseth et al., 2014; Avseth and Veggeland, 2015). Since the background trend in the *AI, Vp/Vs* domain is highly nonlinear due to the complex relationship between compaction and rock-physics properties, Avseth et al. (2014) proposed new equations "*CPEI*- Curved Pseudo Elastic Impedance" and "*PEIL*-Pseudo Elastic Impedance" as fluid and rock stiffness indicators respectively. The authors extracted these attributes consistent with a rock physics template (RPT), taking into account compaction and cementation (Avseth and Veggeland, 2015). Recently, Lehocki et al. (2020) suggested an inversion of the Zoeppritz equation (Zoeppritz, 1919) to obtain the ratio of the density of two layers at the layers' interface. The distinction seemed possible employing the density ratio technique even in (initially) cemented rocks as the diagenetic cement dampens the fluid effect on elastic properties. This technique is in a developing stage and needs testing in other fluid-lithology environments.

The reservoir properties such as porosity, shaliness, and saturation obtained from inverted seismic data (Yenwongfai et al, 2017, 2018) can further be used as input and subsequent calibrations to a 3D reservoir simulation or geomechanical model (e.g., (Herwanger and Koutsabeloulis, 2011). The present study's objective is to deterministically extract the reservoir properties (e.g., porosity, shaliness, permeability) from seismic data using new rock physics equations correlatable with the well log data. The results from work can be used to develop and calibrate a 3D field scale reservoir, and subsequently a geomechanical model for the potential CO_2 storage site Smeaheia in the northern North Sea.

2. Dataset and methodology

A 3D seismic volume GN1101 covering the Smeaheia area, wireline log data from two exploration wells 32/4-1 (Alpha) and 32/2-1 (Beta), and petrographic analysis of Sognefjord Formation sandstone were available for the study. Seismic interpretation carried out by GASSNOVA was also available with the database. We selected the key surfaces (Fig. 1b) for the low-frequency model building before the prestack simultaneous inversion. The complete logs in both wells were gamma-ray curves, whereas, at shallower depths, the sonic and density log data were not recorded. To fill the information against those missing lengths of logs (ranging from 250 m to 800 m), an inversion (Lindseth, 1972) was carried out along the well trajectories starting from the seafloor obtaining the acoustic impedance curves. Using Gardner's equation ($\rho = aV_p^{0.25}$, Gardner et al., 1974), the acoustic impedance data was split in P-wave velocity (*Vp*, in m/s) and bulk density (*RhoB*, in g/cm3), iterating the coefficient 'a' at which the curves splice best with the deeper available *Vp* and density logs. Since the shear wave (*Vs*) logs were not acquired in both the wells, synthetic *Vs* were generated using Greenberg and Castagna (1992) method employing the volume of shale from gamma-ray ($V_{sh}GR$) as input for mineral constrain.

We carried out the prestack inversion using commercial software. The inversion algorithm was based on a modified Fatti et al. (1994) three reflectivity terms (Hampson et al., 2005; Fawad et al., 2020). The available seismic data comprised a set of five partial stacks with angles 0–10°, 10–20°, 20–30°, 30–40°, and 40–50° (Fig. 3a). A preconditioning alignment of traces using a non-rigid method (NRM) was carried out before using these stacks for inversion. After extracting statistical wavelets from all the five partial stacks, both the wells were correlated with the seismic (Fig. 3b). Moderate to good correlation coefficients (0.6–0.7) were obtained. The linear regressions between the acoustic impedance and shear impedance, and acoustic impedance and density were taken as default. The inversion analysis along the wellbore was, however, reasonable within the zone of interest (Fig. 3c).

Finally, the simultaneous inversion was applied on the partial stacks to obtain the acoustic impedance (*AI*), P- to S-wave ratio (*Vp/Vs*), and Density (*RhoB*) cubes (Fig. 4a–c).

A standard petrophysical evaluation was carried out on the logs from both wells 32/4-1 and 32/2-1. The volume of shale (V_{sh}) was calculated by the Clavier method (Asquith et al., 2004) using the gamma-ray log:
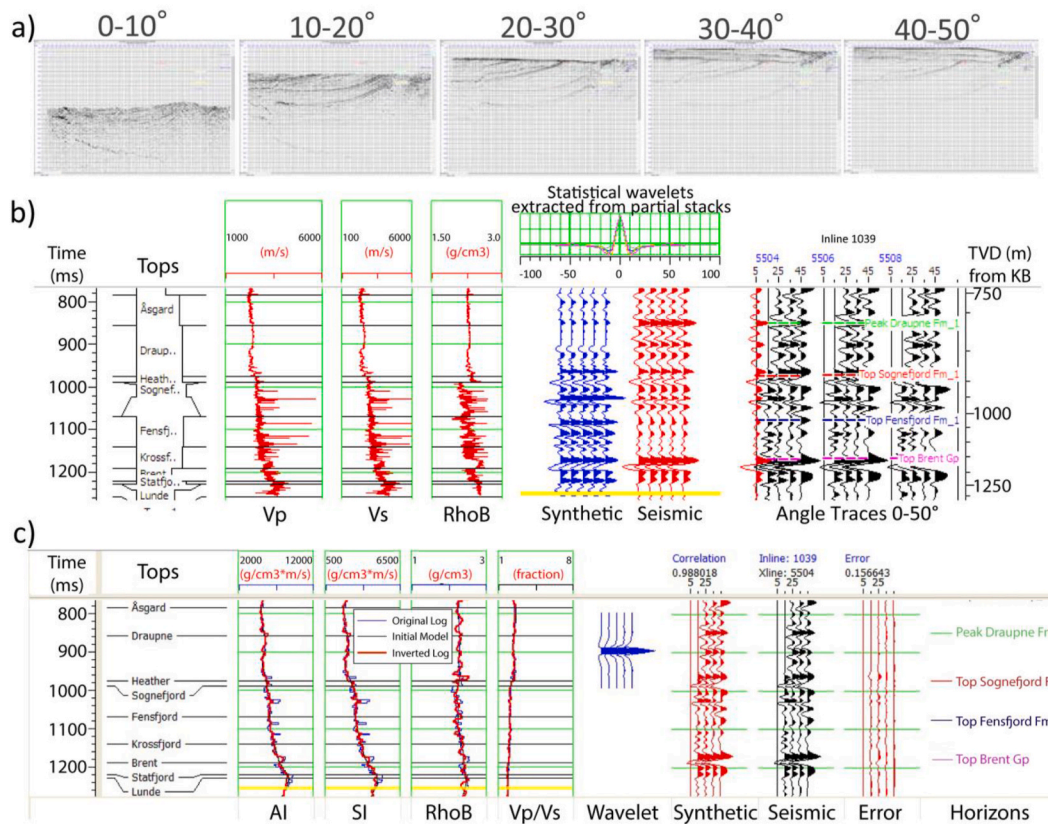
Fig. 3. (a) Angle stacks after preconditioning-alignment of traces using a non-rigid method (NRM). (b) Seismic to well correlation in case of well 32/2-1 showing a moderate to good correlation between the well-synthetic and seismic. (c) Inversion analysis at well (32/2-1) location highlighting the difference of the original elastic properties with the corresponding inverted values.

$$V_{shGR} = 1.7 - \sqrt{3.38 - (I_{GR} + 0.7)^2} \qquad (1)$$

where I_{GR} is the gamma ray index that normalizes the GR curve from 0 to 1 based on the selection of sand and shale lines, respectively.

Effective porosity (φ_e) was calculated using the density (*RhoB*) log with the V_{sh} input. The grain and brine densities were considered 2.65 g/cm3 and 1.02 g/cm3, respectively. Only one core segment in well 32/4-1 was acquired within the Sognefjord Formation (Kinn et al., 1997). The porosity values from the core analysis are slightly higher than the effective porosity (φ_e) estimated from the *RhoB* log (Fig. 5a&b). The permeability was calculated using the φ_e (in fraction) from logs employing a logarithmic-linear form of the equation (PetroWiki, 2021; Timur, 1968):

$$log_{10}k = Clog_{10}\varnothing_e + D, \qquad (2)$$

where k is absolute permeability in millidarcies, coefficients C and D were adjusted to 8.4 and 7.6, respectively, to obtain the permeability comparable to that of the core.

The net reservoir thickness, net-to-gross thickness ratio (*N/G*) were obtained using cut-off $V_{sh} \leq 0.3$, $\varphi_e \geq 0.1$, and permeability (k) > 20mD (Fig. 5). The arithmetic average for each reservoir parameter for both wells (32/4-1 & 32/2-1) is documented in Table 1. Using a nonlinear approach (Avseth et al., 2014; Avseth and Veggeland, 2015), employing a relation between the S-wave velocity and the P-wave velocity (Lee, 2003), we came up with an equation to calculate shale volume (V_{sh}) based on the *AI, Vp/Vs* ratio domain.

$$V_{sh} = \frac{\left\{ \rho_{ma} - \dfrac{AI}{V_{Pma}} - \left[1 - \left(\dfrac{V_S}{V_P G \alpha} \right)^{\frac{1}{n}} \right] \left[AI \left(\dfrac{1}{V_{Pw}} - \dfrac{1}{V_{Pma}} \right) - (\rho_w - \rho_{ma}) \right] \right\}}{\left[(\rho_{sh} - \rho_{ma}) - AI \left(\dfrac{1}{V_{Psh}} - \dfrac{1}{V_{Pma}} \right) \right]},$$

$$\qquad (3)$$

where V_{sh} is the volume of shale in fraction, *Phi* is porosity in fraction, *AI* is acoustic impedance in g/cm^3*m/s, V_P is P-wave velocity in m/s, V_S is S-wave velocity in m/s, G is mineralogy/shaliness coefficient, α is Vs/Vp ratio of the mineral/rock matrix, n is stress/cementation coefficient, V_{Pma}, V_{Psh} and V_{Pw} are the P-wave velocities (in m/s) of the mineral matrix (e.g., quartz), shale and water respectively, ρ_{ma} is the density of mineral grains, ρ_{sh} is the density of shale, ρ_w is the density of water (all in g/cm3). Equation (3) is based on a three component system, defined by a matrix pole (e.g., quartz), shale pole and a water pole (Fig. 6). Changing the mineralogy/shaliness coefficient 'G' results in a vertical static shift in the iso-V_{sh} contours (Fig. 6), that we selected 1.02 for well 32/4-1, and 0.99 for 32/2-1. The stress/cementation coefficient 'n' controls the slope of the iso-V_{sh} contour lines and is selected (n = 0.55 in our case) such that the line with $V_{sh} = 0$ calibrates with the brine saturated sandstone trend from the well data. The matrix and fluid-related constants may be taken from Mavko et al. (2009) and vendors' logging chart books. The values of V_{Psh} and ρ_{sh} define the shale pole constraining the $V_{sh} = 1$ contour on the *AI, Vp/Vs* plane.

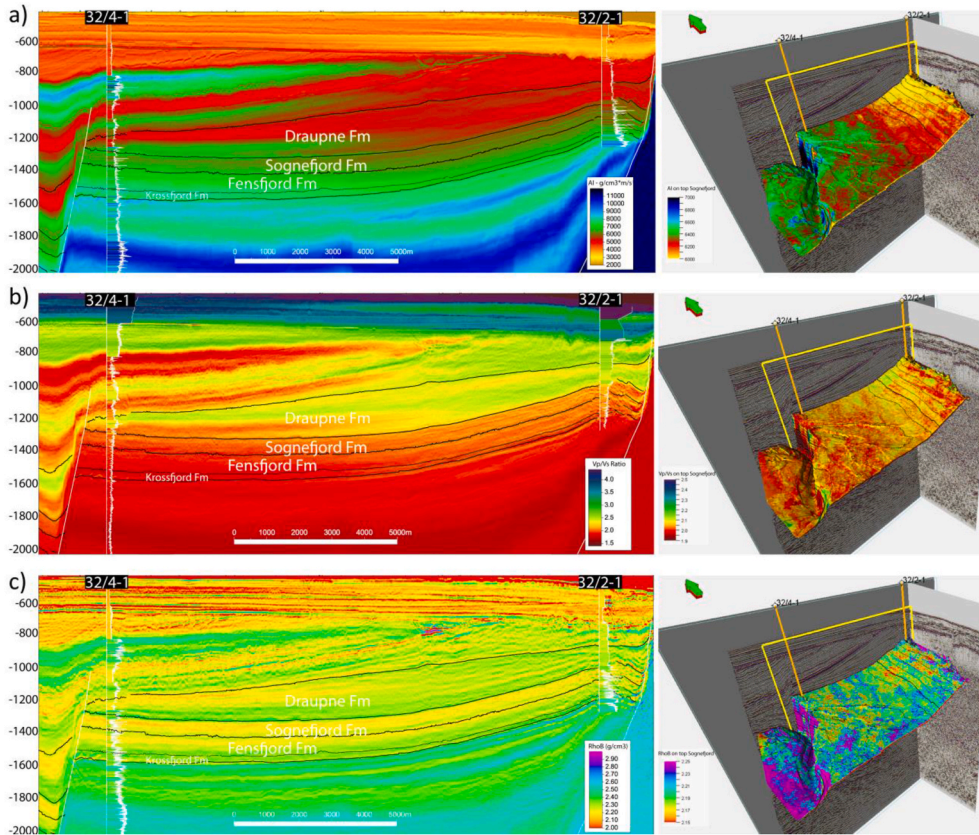A variant of Equation (3), modified empirically to calculate porosity using *AI, Vp/Vs* information, is:

Fig. 4. Profiles from the prestack inverted cubes (a) *AI*, (b) *Vp/Vs* Ratio, and (c) *RhoB*. The corresponding properties displayed on the top Sognefjord TWT surface are placed on the right, with the profile locations highlighted by yellow rectangles. (For interpretation of the references to color in this figure legend, the reader is referred to the Web version of this article.)
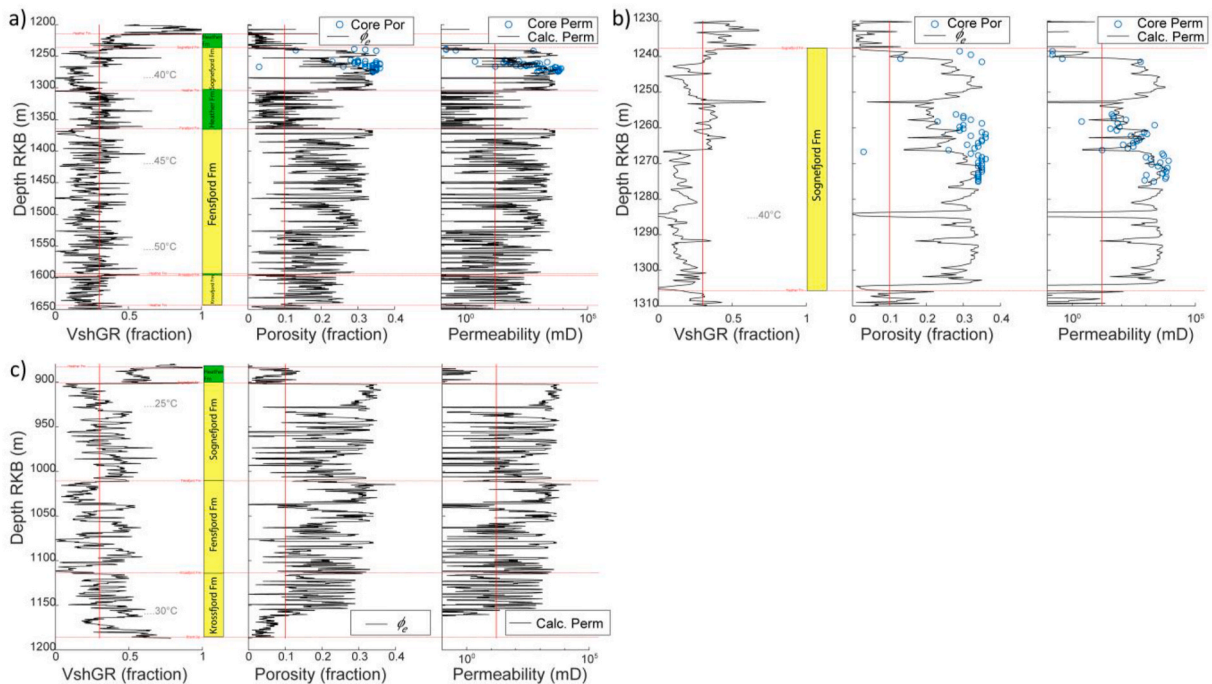

Fig. 5. Reservoir parameters plotted against depth with corresponding cut-off lines (red), (a) Shale volume (Vsh_{GR}), effective porosity (φ_e), and permeability (k) calculated using petrophysical methods from logs in well 32/4-1 with the porosity and permeability data measured in the core (Kinn et al., 1997, blue circles). (b) Same plot showing Sognefjord Formation only, (c) $V_{sh}GR$, φ_{e}, and k calculated using petrophysical methods from logs in well 32/2-1. (For interpretation of the references to color in this figure legend, the reader is referred to the Web version of this article.)

Table 1
Reservoir zones and the corresponding average parameters obtained from the petrophysics analysis.

| Zone Name	Top	Bottom	Gross	Net	N/G	Av Phi	Av Sw	Av Vsh	Av Perm	Phi*H	Vsh*H
	m	m	m	m	fraction	fraction	fraction	fraction	mD	m	m
	MDRKB	MDRKB									
Well 32/4-1											
SOGNEFJORD FM	1238	1306	68	48.88	0.72	0.30	1.0	0.16	2039	14.5	8.0
FENSFJORD FM	1366	1595	229	135.11	0.59	0.26	1.0	0.19	921	35.2	25.3
KROSSFJORD FM	1598	1645	47	23.77	0.51	0.21	1.0	0.18	130	5.1	4.4
All Zones	1238	1645	344	207.77	0.60	0.26	1.0	0.18	1094	54.7	37.6
Well 32/2-1											
SOGNEFJORD FM	902	1012	110	39.11	0.36	0.31	1.0	0.23	2989	12.2	8.9
FENSFJORD FM	1012	1115	103	53.25	0.52	0.28	1.0	0.18	1729	15.1	9.5
KROSSFJORD FM	1115	1187	72	11.89	0.17	0.25	1.0	0.24	511	2.9	2.8
All Zones	902	1187	285	104.24	0.37	0.29	1.0	0.20	2063	30.3	21.2
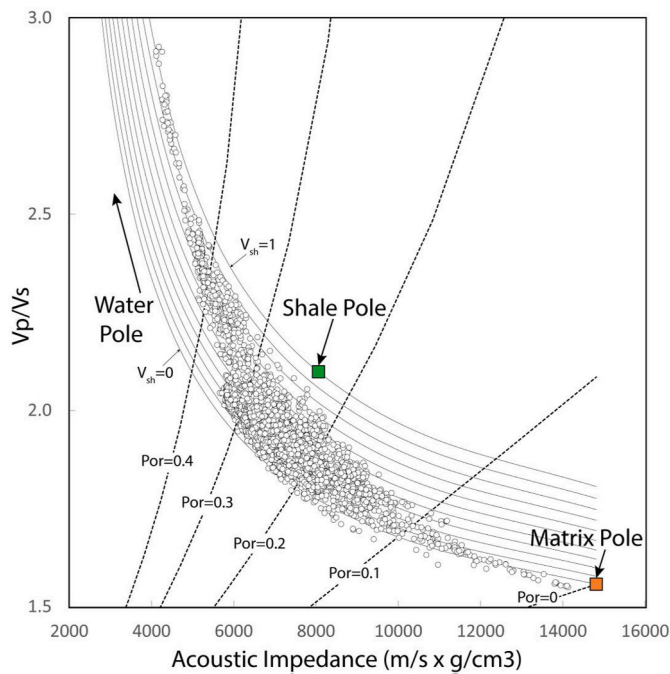
Fig. 6. Well 32/4-1 data plotted on an *AI*, *Vp/Vs* plane with iso-V_{sh} and iso-porosity contours computed using Equations (3) and (4) respectively. Positions of the three components (Matrix, Shale, and Water) are indicated accordingly.

$$Phi = 1 - \frac{0.001429AI - J - \left[1 - \left(\frac{V_s}{V_p G\alpha}\right)^{\frac{1}{n}}\right][0.00024AI + J - 1]}{\left[(\rho_{ma} - J) - AI\left(\frac{1}{V_{Pma}} - 0.001429\right)\right]}, \quad (4)$$

where *Phi* is porosity in fraction, and J is calibration coefficient (with values 1 to 4) that laterally moves the iso-porosity contours, with zero porosity contour anchored on the matrix pole (Fig. 6). There is a patent-pending on the quantification procedure related to Equation (3). Derivations and other related details of these equations will be presented in a subsequent publication. We generated *G* cube with a transition of values from well 32/4-1 to 32/2-1 and subsequently using Equation (3) and Equation (4) by putting the *AI* and *Vp/Vs* cubes, obtained the V_{sh} and *Phi* cubes, respectively. The porosity was calculated using Equation (4) only in zones with V_{sh} below 0.3. Permeability (*k*) cube from porosity (*Phi*) cube was extracted using Equation (2). Finally, using the V_{sh} cube, we extracted sand depositional geometries to get an insight into the depositional environments.

We performed exhumation estimates on wells 32/4-1 and 32/2-1, comparing the *Vp* data with experimental compaction trends of 50:50

silt-kaolinite mixture (Hansen et al., 2017; Marcussen et al., 2010) and reconstituted Etive Sandstone (Marcussen et al., 2010).

Furthermore, a rock physics evaluation was carried out to relate the reservoir properties with the depositional environment and diagenesis, employing well log data on the *RhoB-Vp* plane (Avseth et al., 2005). The critical porosity was assumed according to the data distribution at low density/high porosity. In a transitional depositional environment, the water density was considered to be 1.02 g/cm^3.

3. Results and discussion

3.1. Comparison between seismic-derived and well log-based reservoir parameters

The Sognefjord Formation in well 32/2-1 has a gross thickness of 110 m with an average porosity of 0.31. The thickness and porosity within the Sognefjord Formation decrease towards the west in well 32/4-1 (thickness 68 m and porosity 0.30 respectively); however, the net-to-gross thickness ratio (*N/G*) 0.36 is low in well 32/2-1 compared to 0.72 in well 32/4-1 (Table 1). The Fensfjord Formation in well 32/2-1 has a gross thickness of 103 m and *N/G* 0.52 lower than in well 32-4-1 (i.e., thickness 229 m and *N/G* 0.59 respectively). The Fensfjord Formation average porosity is 0.28 in well 32/2-1, which is slightly better than in well 32/4-1 (0.26). The Krossfjord Formation generally exhibits poor reservoir properties in both wells. In well 32/2-1 the Krossfjord is comparatively thin (gross thickness 72 m), with a high average porosity (0.25) compared to a lower gross thickness of 47 m and porosity 0.21 in well 32/4-1. The Krossfjord Formation *N/G*, however, is a lot better (*N/G* 0.51) in well 32/4-1 compared to that of in well 32/2-1 (0.17). The average permeability is generally higher in the Sognefjord, Fensfjord, and Krossfjord formations in well 32/2-1.

The V_{sh} values calculated using the *AI* and *Vp/Vs* logs matched well with the V_{sh} extracted from the gamma-ray log (i.e., $V_{sh}GR$) except for some over-prediction within the Draupne Formation in well 32/4-1 (Fig. 7a). The porosity values calculated from the *AI, Vp/Vs* showed a good fit with the effective porosity (φ_e) derived from the density log. There is some porosity over prediction within the lower part of the Krossfjord Formation in well 32/2-1 (Fig. 7b). Both the V_{sh} and φ_e calculations from traditional petrophysics generally show a good correlation with the respective properties calculated using rock physics models (i.e., Eqs. (3) and (4)), except in the case of low porosity, which the rock physics method slightly overpredicts (Fig. 7c and d).

Extracting the inverted cubes within a 25 m distance around both wells (32/4-1 & 32/2-1) show that the *AI* and *Vp/Vs* have restricted distribution compared to the same data from well logs on the *AI, Vp/Vs* plane (Fig. 8a–e). This is due to the difference in the resolution of the well logs and seismic data. The V_{sh} value distribution is similar to that from the well logs in the *AI, Vp/Vs* plane (Fig. 8a–b). The porosity cube extracted using Equation (4) shows a better match with the well log porosity than that calculated from the *RhoB* cube (Fig. 8c–e).
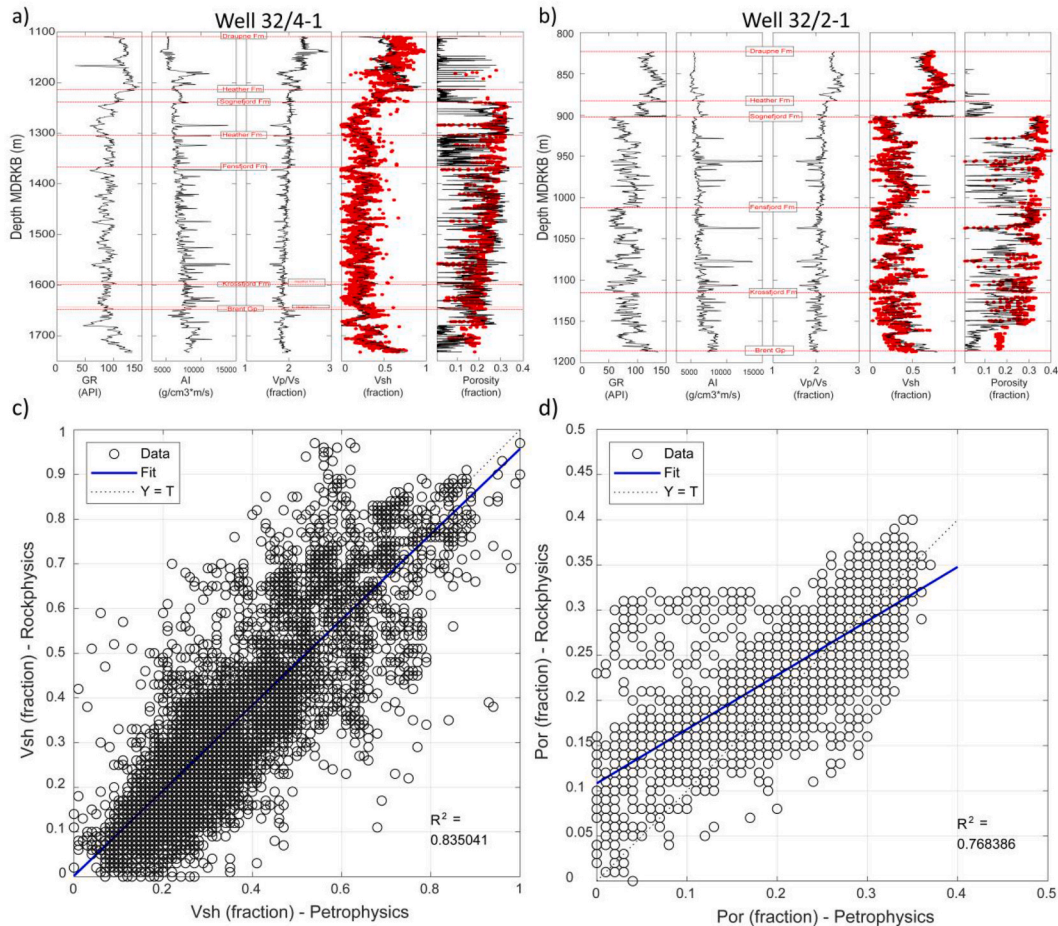
Fig. 7. Comparison between V_{sh} extracted using Equation (3) (red points), V_{sh} from gamma ray log (black line), *Phi* extracted from Equation (4) (red points), and φ_e from density log (black line) in (a) well 32/4-1 and (b) well 32/2-1. (c) Comparison between V_{sh} computed from *GR* log using a petrophysical method and the V_{sh} from the rock physics-based Equation 3, (d) φ_e calculated from the *RhoB* log using petrophysics versus *Phi* from the rock physics based Equation (4). (For interpretation of the references to color in this figure legend, the reader is referred to the Web version of this article.)

3.2. Rock physics analysis of the potential reservoir sands

We carried out a rock physics analysis to further investigate the relationship between elastic properties (i.e., velocity and density) and reservoir properties such as porosity, cementation, and shale volume. The objective was to infer the degree of influence of these reservoir properties on the seismic-derived attributes. Considering the section from top Draupne Formation to top Brent Group in both wells (32/4-1 and 32/2-1) that comprises the Sognefjord, Fensfjord, and Krossfjord formations, there are numerous spikes in the *Vp* and *RhoB* logs (Fig. 9a and c). These are a possible manifestation of carbonate laminations, as the carbonate minerals owe high P-wave velocity and density. The reservoir sands are at a present-day temperature ranging from 40 to 50 °C in well 32/4-1 (Fig. 9a); however, the data plotting above the constant cement line on the *RhoB-Vp* plane indicates a higher paleo-temperature regime (Fig. 9b). Some missing data points within the Draupne Formation were infilled using Gardner's equation that is manifested as a linear trend on the *RhoB-Vp* plane, signifying the limitations of using synthetic data. In well 32/2-1, the zone of interest lies between present-day temperature 25–30 °C (Fig. 9c), while the absence of cementation on the *RhoB-Vp* plane confirms that the sands stayed within the mechanical compaction zone since deposition (Fig. 9d).

The Sognefjord Formation sandstone is possibly well sorted when deposited as the data plots on a high porosity against low Vp values. To include the high porosity data under the contact cement line, a high critical porosity ($\varphi_c = 0.44$) was selected for the contact cement line

calculation on the *RhoB-Vp* plane (Fig. 10a). The well 32/2-1 data falls below the constant cement line indicating the zone falling within the mechanical compaction zone. Several of the cleanest sand data points in well 32/4-1 generally plot above the constant cement line showing the formation has been exposed to a temperature (~70 °C), higher than the present-day temperature. Assuming the present-day North Sea temperature gradient (i.e., 35 °C/km), it can be inferred that the maximum burial depth of the area around well 32/4-1 was more than the present depth of 700 m. This assertion is confirmed by the uplift analysis that reveals 1100 m uplift for the well 32/4-l (Fig. 11a). The uplift increases towards the east in well 32/2-1, i.e., 1300 m (Fig. 11b). In both the wells, no overpressure has been reported; furthermore, there is a scatter of high density, high-velocity points indicating the presence of thin carbonate cemented intervals (Fig. 10a).

The Fensfjord Formation sandstones are similar to the Sognefjord Formation sandstones in terms of sorting. Most of the cleanest sandstone data in well 32/4-1 fall above the constant cement line indicating exposure to temperatures higher than 70 °C (Fig. 10b). The high density, high velocity scattered points indicate carbonate-bearing intervals in both the wells (32/4-1 & 32/2-1). The Fensfjord Formation data in well 32/2-1 plots below the constant cement line signifying that the formation in the study area possibly remained within the mechanical compaction zone since deposition.

The Krossfjord Formation, in contrast to the type section (NPD, 2020), is possibly poorly sorted in this area. Therefore, to constrain the data, the critical porosity is assumed to be lower ($\varphi_c = 0.4$) than the
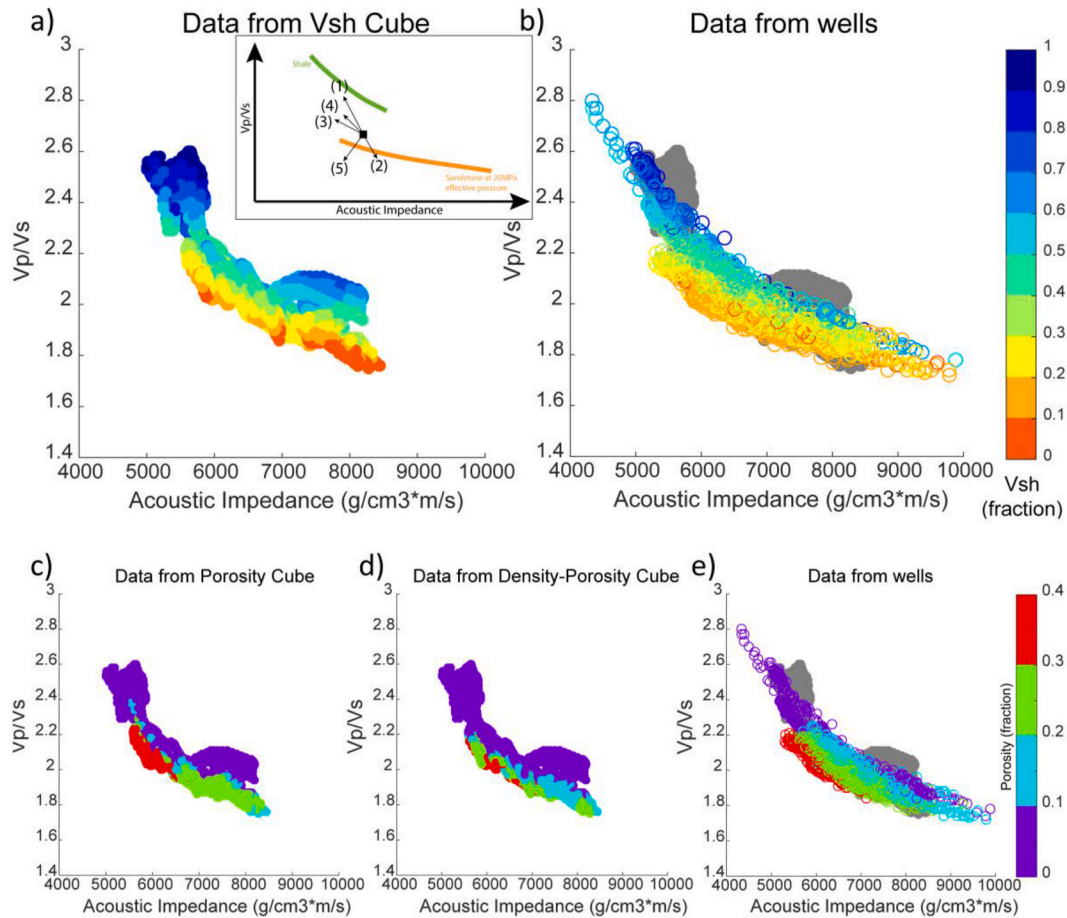
Fig. 8. (a) Comparison between the inverted cube data extracted within a distance of 25 m around the two wells (32/4-1 and 32/2-1) with the properties obtained from well logs onto the *AI, Vp/Vs* plane (a) V_{sh} extracted from the prestack inversion, (b) $V_{sh}GR$ points overlapping the inverted data points (gray), (c) *Phi* extracted from the inverted data using Equation 4, (d) *Phi* calculated from the inverted density cube, and (e) φ_e obtained using *RhoB* logs overlapping the inverted data points (gray). The inset in (a) does also show how the brine saturated sandstone will plot as the (1) shale content increase, (2) the amount of cement increase, (3) the porosity in the sandstone increase, (4) the effective pressure in the formation decrease and (5) the saturation of gas increasing relatively to the saturation of hydrocarbon within the sandstone (Avseth et al., 2005).

shallower formations (Fig. 10c). The formation in well 32/2-1 is unclean with shale intercalations; however, as the zone becomes deeper towards the well 32/4-1, the sands are cleaner with a high level of cementation. Few high density, high-velocity points indicate thin carbonate laminations. As expected, the formation possesses overall low porosity compared to the shallower Fensfjord and Sognefjord Formations.

3.3. Seismic-derived reservoir properties

The maximum magnitude of reservoir parameters extracted from the inverted seismic data within the respective interval of Sognefjord, Fensfjord, and Krossfjord formations showed that the best sand ($V_{sand}>0.9$ or $V_{sh}<0.1$) is present in the east with a north-south strike (Fig. 12a–c). This feature is very prominent in the Sognefjord Formation (Fig. 12a), which seems to shift southwards in the deeper Fensfjord and Krossfjord Formations (Fig. 12b–c). The porosity calculated using Equation (4) shows a systematic decrease from east to west in all the three Sognefjord, Fensfjord, and Krossfjord formations (Fig. 12a–c). Also, there is an overall porosity decrease from Sognefjord Formation to the deeper Fensfjord and Krossfjord Formations. The porosity estimated using the *RhoB* cube also shows a similar decrease of porosity in deeper formations, with Sognefjord Formation sandstone exhibiting the best overall porosity. The lateral change in porosity with depth within a formation is not so prominent in the *PhiD* attribute compared to *Phi* (Fig. 12a–c).

The average magnitude of the reservoir properties has limitations owing to the low seismic resolution compared to the wireline logs; however, it may yield useful information. The Sognefjord Formation shows an average V_{sh} of ~0.3 that decreases in the northeast towards the well 32/2-1 (Fig. 13a). The sands are generally homogenous over the area. The average porosity in both *Phi* and *PhiD* calculations seems to be high (~0.28) in the middle of the area, which is somehow influenced by the NW-SE running faults. The average V_{sh} range within the Fensfjord Formation is similar to the Sognefjord Formation except for some high sand anomalies (V_{sh}~0.2) in the middle and southeast of the area (Fig. 13b). Both *Phi* and *PhiD* show higher porosity values (~0.28) in the middle of the area. The average V_{sh} in Krossfjord Formation is low (~0.20) in some patches, which possibly represent various sand bodies deposited in the area (Fig. 13c). The *Phi* calculations show a relatively better porosity in the northeast (~0.27), whereas the overall porosity in the *PhiD* map is low and patchy.

The highest permeability (~2000 mD) in Sognefjord Formation lies in the east; however, the average permeability anomaly (<1000 mD) is exhibited in the middle and southeast of the area (Fig. 14a). Since permeability is derived from the porosity (*Phi*), there is a permeability distribution controlled by faults as in the case with porosity (Fig. 13a). The Fensfjord Formation permeability increases towards the east, manifested by both the maximum and average magnitude maps. The overall permeability values are, however, lower than the Sognefjord Formation permeability (Fig. 14b). The Krossfjord Formation
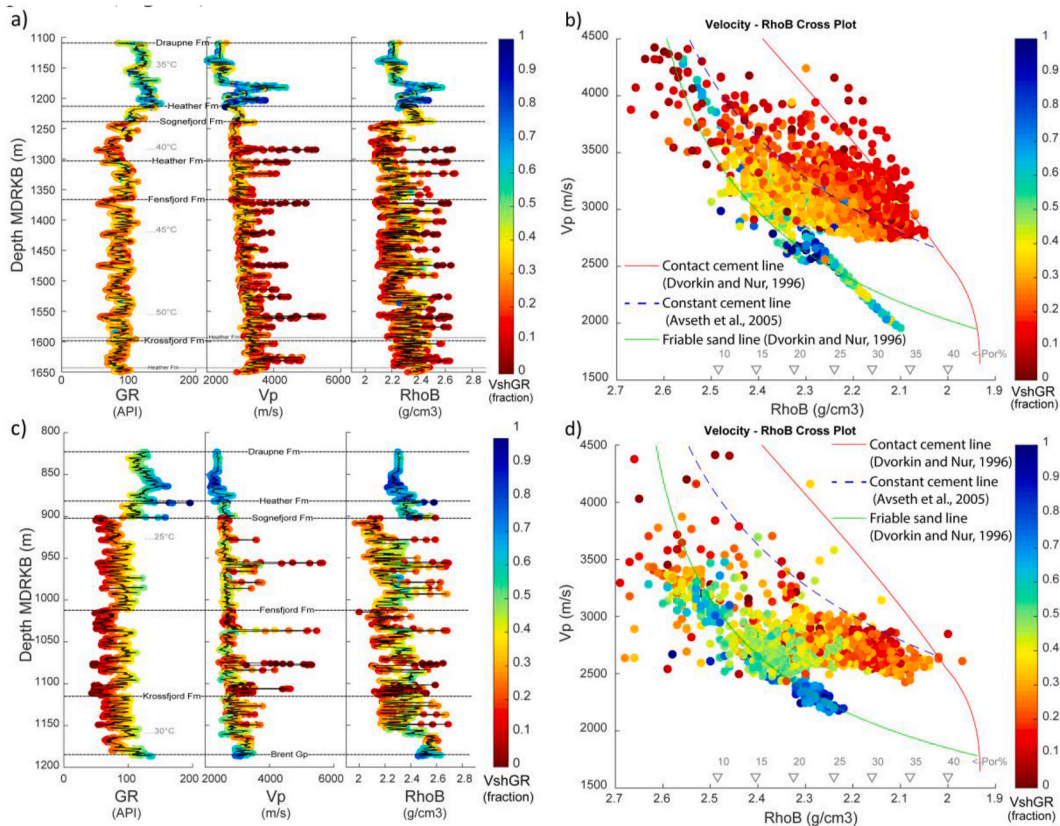
Fig. 9. Well log data from Top Draupne Formation to Top Brent Group color-coded with $V_{sh}GR$ (a) GR, Vp, and $RhoB$ values in well 32/4-1 plotted against depth. (b) $RhoB$-Vp crossplot (in well 32/4-1) with (red) contact cement line (Dvorkin and Nur, 1996), (blue stippled) constant cement line (Avseth et al., 2005), and (green) friable sand line (Dvorkin and Nur, 1996). The linear trend represents the data within Draupne Formation generated using Gardner's equation. (c) Well 32/2-1 GR, Vp, and $RhoB$ values plotted against depth. (d) $RhoB$-Vp crossplot (in well 32/2-1) with contact cement line (Dvorkin and Nur, 1996), constant cement line (Avseth et al., 2005), and friable sand line (Dvorkin and Nur, 1996). The spikes in Vp and $RhoB$ (a and c) are possible carbonate cemented zones. (For interpretation of the references to color in this figure legend, the reader is referred to the Web version of this article.)
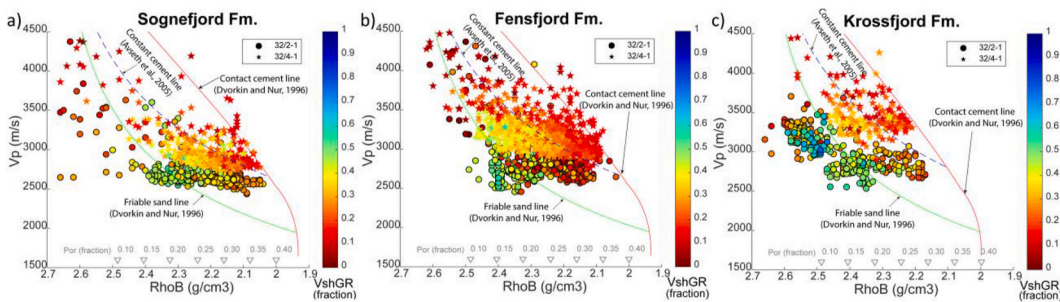

Fig. 10. $RhoB$-Vp crossplots with contact cement line (Dvorkin and Nur, 1996), constant cement line (Avseth et al., 2005), and unconsolidated sand line (Dvorkin and Nur, 1996) for (a) Sognefjord Formation, (b) Fensfjord Formation and (c) Krossfjord Formation.

permeability in the maps show maximum and average magnitude permeability increasing towards the east; however, the overall values are lower than that of the Sognefjord and Fensfjord Formations (Fig. 14c).

On a profile (inline-1266) from the V_{sand} $(1-V_{sh})$ cube, the cleanest sands (V_{sh}<0.1) are present on the easternmost part within the Sognefjord Formation, whereas there are some lens-shaped bodies interpreted to be possible point bars within the lower part of the Krossfjord Formation (Fig. 15a). Occasional point bars are also present in the lower part of the Fensfjord Formation. Using the clean sand data points (with cutoff V_{sh}<0.1), 3D litho-bodies were generated (Fig. 15b). The bodies connecting the point bars assumed a shape interpreted to be deltaic. The north-south striking sand body, also exhibited in Fig. 12, is interpreted

to be deposited in a shoreface/beach setting. A northward shift of the strike of the sand body from deep to shallow formations is evident here. These findings support previous studies where spit to the deltaic depositional environment was reported in Troll area for the Sognefjord, Fensfjord and Krossfjord formations (Dreyer et al., 2005; Holgate et al., 2015). The *Phi* profile shows the highest overall porosity within the Sognefjord Formation (Fig. 16a), whereas the *PhiD* profile shows overall high porosity within both the Sognefjord and Fensfjord Formations and relatively low porosity within the Krossfjord Formation (Fig. 16b). One interesting feature in both *Phi* and *PhiD* attributes is that the porosity within the possible delta-related deposits/point bars is comparatively low.
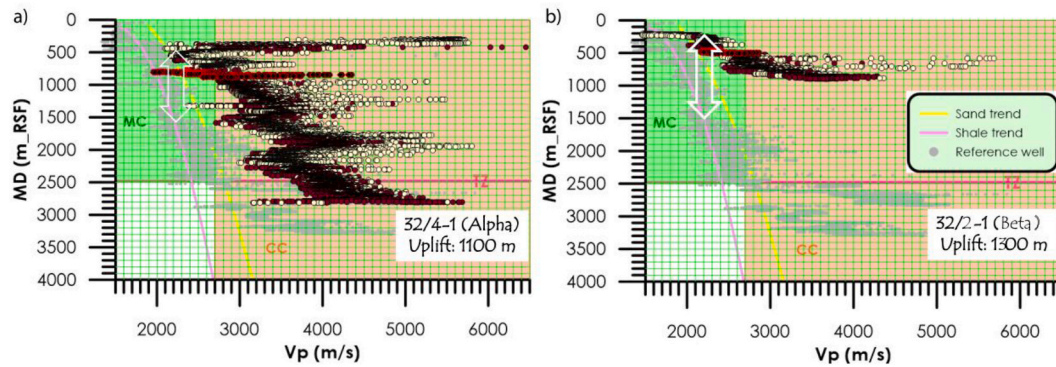
Fig. 11. Uplift estimation by comparing the well log *Vp* data with that of reference sand and shale trends (Hansen et al., 2017; Marcussen et al., 2010; Mondol et al., 2008b). A reference North Sea well with normal compaction and zero-uplift is also plotted (grey points). (a) The well 32/4-1 shows an uplift ~1100 m, (b) the well 32/2-1 shows an uplift ~1300 m. RSF: Reference from the Seafloor, MC: Mechanical Compaction, CC: Chemical Compaction, TZ: Transition Zone.
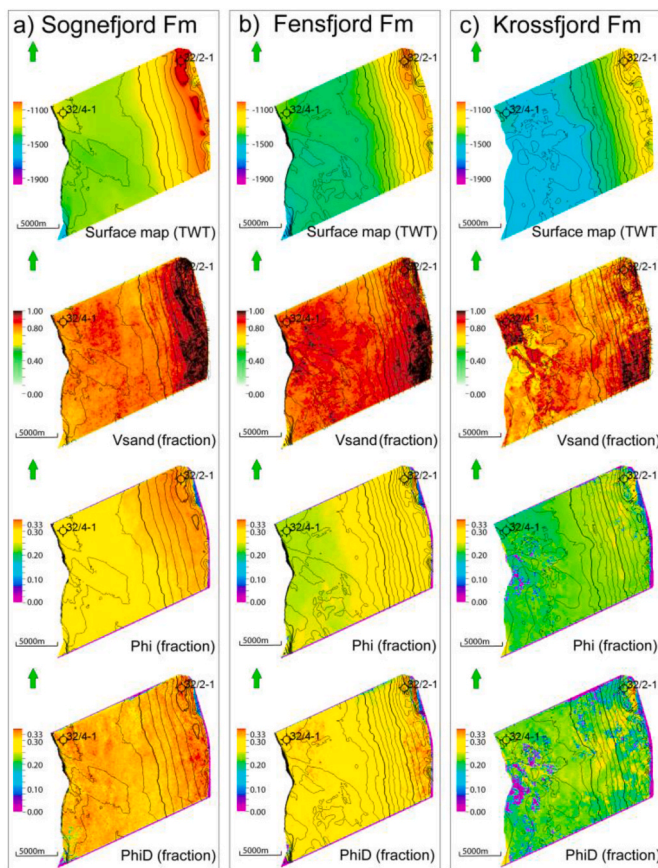

Fig. 12. TWT surface maps and maximum magnitude of reservoir properties extracted from the inverted cubes within (a) Sognefjord Formation, (b) Fensfjord Formation, and (c) Krossfjord Formation.

3.4. Smeaheia sandstone reservoirs as potential CO_2 storage candidates

The buoyancy trapping is the main process for CO_2 storage during the injection and the subsequent early stage of storage (Riley, 2010). Therefore, CO_2 injection is carried out at the base of the reservoir, and the plume moves laterally within the most permeable layers until it finds a vertical conduit to move vertically upwards. The plume behavior depends on the subtle horizontal and vertical heterogeneities within the reservoir, which are adequately reflected in the physical properties. The lateral continuation of thin clay and silt layers or carbonate laminations may help lateral distribution of CO_2 in the storage, until the plume finds

a vertical permeable zone to move and accumulate below the caprock base. One example is the Sleipner GCS project, where the time-lapse seismic enables one to identify and delineate the migration path and subsequent accumulation of the CO_2 plume (Chadwick et al., 2004). Therefore, predicting the CO_2 plume behavior from seismic-derived properties in addition to the wireline log information is essential, keeping in mind the issues of the low resolution of seismic.

The reservoir sandstones in the Smeaheia area appear to be sheet-like in the *Vsand* profile extending from the well 32/4-1 to 32/2-1 (Fig. 15a); however, looking at the logs, the sandstones exhibit coarsening upward cycles indicating progradation (Fig. 2b). The shoreface/beach depositional system prograded westwards, forming continuous sand sheets, can be potentially excellent reservoirs for geological CO_2 sequestration. The shoreface sands seem to be shifting along the strike gradually northwards from the older Krossfjord to the younger Sognefjord Formations (Fig. 12a–c). Towards the west, there are possible deltaic sands, mainly in the Krossfjord Formation and partially in the Fensfjord Formation with the source possibly from the north. These sands are very clean but possess comparatively low porosity that could be attributed to a moderate level of cementation for being deep in stratigraphic succession, possibly with not enough chlorite coatings on the quartz grains (Ehrenberg, 1993). A further analysis focussing on the three reservoir sandstones is given below:

3.4.1. Sognefjord Formation

Minor shale beds separate the Sognefjord sandstones in both wells 32/4-1 and 32/2-1 (Fig. 2b). The shales are somehow identifiable, especially in the east, towards well 32/2-1 in the V_{sand} cube, where the shale thickness is more than the seismic resolution (Fig. 15a). Our rock physics analysis indicates that while deposition, the sands were well sorted with high initial porosity. Since the eastern part of the area, towards well 32/2-1, has always been within the mechanically compacted zone (Fig. 11b), the porosity and permeability are excellent, as evident in Figs. 12 and 14. The eastern side uplifted about 1300 m for being closer to the continental mass. The average porosity (both *Phi* and *PhiD*) is misrepresented as the interval average takes into account the effective shale porosity ($\varphi_{sh\sim}0$), which results in a reduction of the porosity where the shale thickness is above the seismic resolution. In the west, towards well 32/4-1, the formation experienced quartz cementation, especially the clean sandstones show a higher level of cementation (Fig. 10a). This implies that the western side has been exposed to a minimum temperature of 70 °C at maximum burial depth, indicating a subsequent uplift of around 1100 m (Fig. 11a). The porosity in the western part is also good, as recorded in well 32/4-1 (Table 1) and also from the seismically derived porosities, i.e., *Phi* and *PhiD* (Figs. 12a and 13a).

The 32/4-1 well core analysis (Martin and Lowrey 1997) shows fine to very fine-grained, well-sorted with moderate to good quality Sognefjord sandstone (Fig. 17). The intermediate permeability (~602mD)
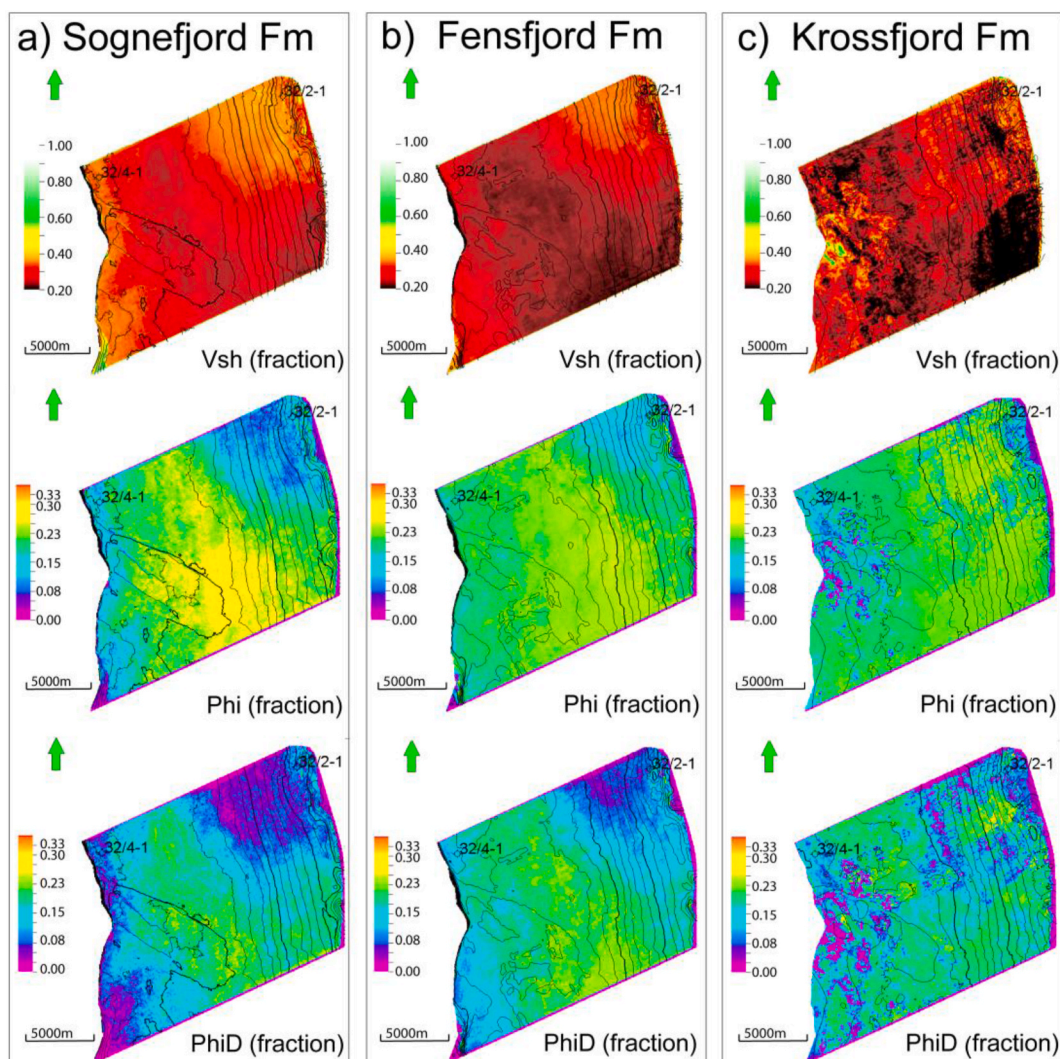
Fig. 13. The average magnitude of reservoir properties extracted from the inverted cubes within (a) Sognefjord Formation, (b) Fensfjord Formation, and (c) Krossfjord Formation.

sandstone contains an open porosity network and good pore connectivity (Fig. 17a). The undeformed muscovite mica flakes (Fig. 17a) indicate a low compaction level. The comparatively low permeability (~70mD) can be attributed to small pore sizes and associated narrow pore throats, although the sandstone owes abundant and well-connected porosity (Fig. 17b). The preferred orientation of elongated grains indicates a comparatively higher compaction level. The high permeability sandstone (~4600 mD) contains slightly larger pores (up to 100 μm diameter) with excellent connectivity through widespread clean and open pore throats (Fig. 17c). A zoomed view of this high permeability sandstone reveals the presence of some pore-filling Kaolinite occasionally located within a grain dissolution pore (Fig. 17d). The secondary porosity is generated through the dissolution of K-Feldspar grains and overgrowths (Fig. 17d). These samples are at the present depth of 1241–1268 m (MDRKB), and the thin section images confirm that these sandstones lie mainly within the mechanical compaction zone with no significant influence of chemical compaction. Kaolinite clays do not swell as much as Smectites in the presence of water to reduce porosity and permeability. However, migration of clay grains could plug the pore-throats while a CO_2 injection, potentially reducing permeability in a high amount of kaolinite-bearing sandstone (Aksu et al., 2015).

The permeability barriers due to the presence of carbonate stringers (Fig. 9a and c) are too thin to detect on seismic-derived data, which may provide resistance in a vertical CO_2 flow; however, these features can

also help regulate the injected CO_2 for better lateral distribution (Sundal et al, 2013, 2016).

3.4.2. Fensfjord Formation

The Fensfjord Formation sandstones also exhibit a sheet-like deposition by the prograding shoreface; however, there are few sand bodies possibly of deltaic origin in the middle of the Smeaheia area (Fig. 12b), likely in the lower part (Fig. 15a). The overall porosity (>0.25) and permeability (~1000 mD) are good, generally increasing in the east towards well 32/2-1 (Table 1, Figs. 12b and 14b) for being within the mechanically compacted zone (Figs. 10b and 11b). However, the average porosity maps show high porosity in the middle due to the presence of low V_{sh} in that area (Fig. 13b). Similar to the Sognefjord Formation, there are carbonate related permeability barriers within the Fensfjord Formation (Fig. 9a and c), which could be helpful in a lateral CO_2 distribution (Sundal et al, 2013, 2016).

3.4.3. Krossfjord Formation

The Krossfjord Formation sandstones are discontinuous, separated by several sand bodies (Figs. 12c and 13c). The southeastern corner of the area contains a prominent sand anomaly that is deposited possibly in a shoreface environment. In the west, the deposition is possibly delta related (Fig. 15a–b); however, these clean sands are quartz cemented, exhibiting a moderate porosity (Fig. 10c and 16a-b). The low gross
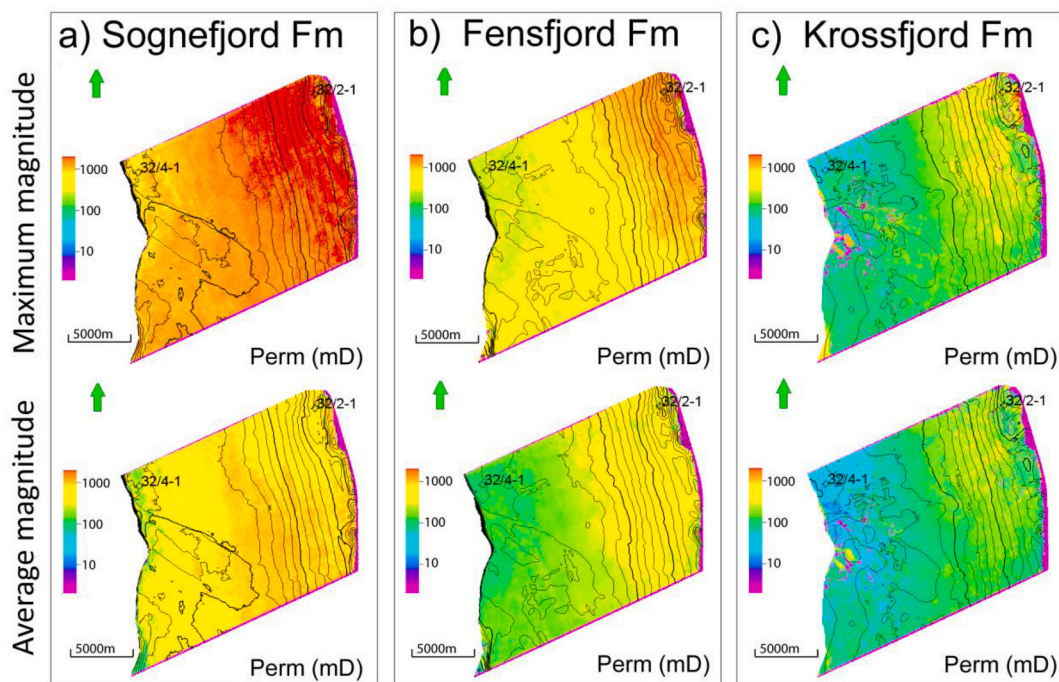
Fig. 14. The maximum and average magnitude of reservoir permeability extracted from the Phi cubes within (a) Sognefjord Formation, (b) Fensfjord Formation, and (c) Krossfjord Formation.
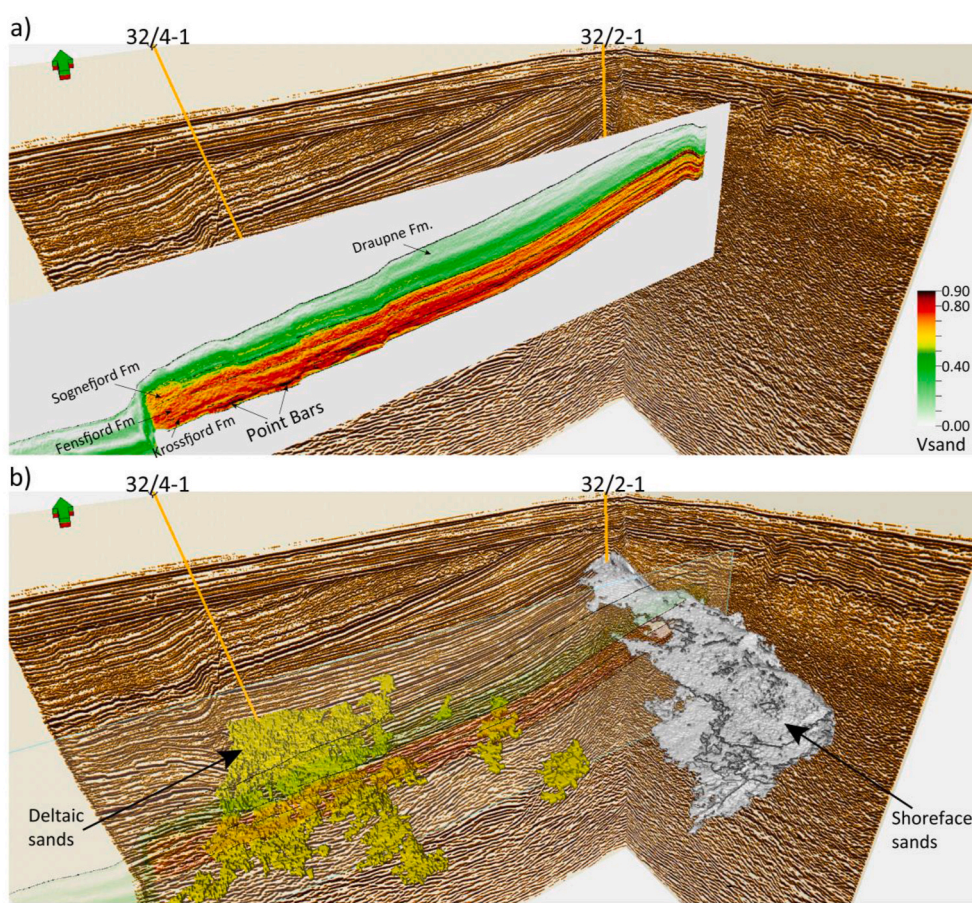

Fig. 15. (a) V_{sand} profile (inline-1266) showing possible point bars where the sand is very clean ($V_{sh}<0.1$). (b) Sand bodies extracted using the clean sand data reveal two main depositional geometries, i.e., possible shoreface/beach and deltaic depositional environments. The shoreface/beach sands prograded westwards, forming continuous sand layers within all the three Sognefjord, Fensfjord, and Krossfjord formations accordingly (a).
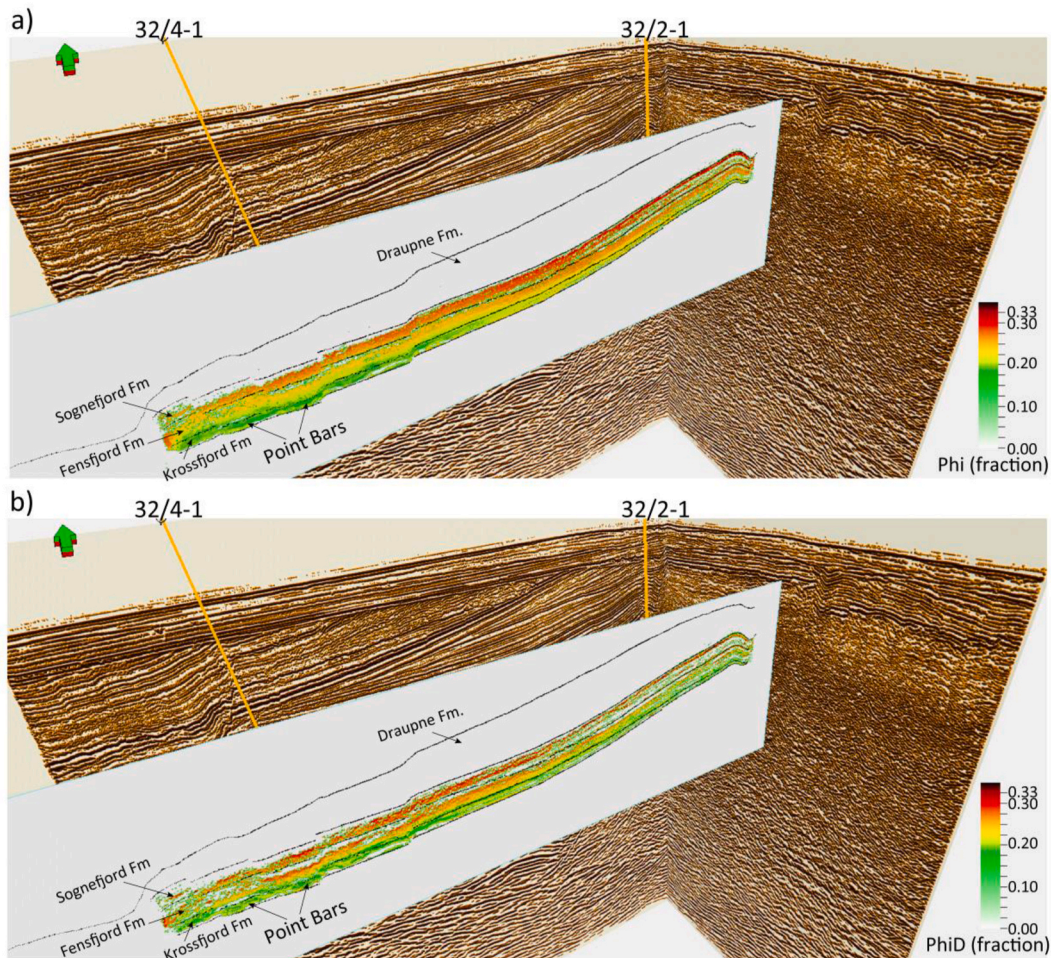
Fig. 16. (a) Inline-1266 showing porosity (a) calculated from the inverted seismic data using Equation (4) and (b) calculated from the inverted *RhoB* cube. The delta-related sands (point bars) exhibit relatively low porosity in the profiles from both the porosity extraction methods.

thickness and *N/G*, high shaliness, moderate porosity, and permeability, uncertainties in the sand body connectivity make the Krossfjord Formation a less likely candidate for CO_2 storage.

3.5. Limitations and pitfalls

Assuming a frequency of 40 Hz with an average seismic velocity of 2600 m/s, the vertical seismic resolution around this depth is approximately 16 m in the Smeaheia area. Therefore, extracting meaningful reservoir properties in sandstones with thickness below the seismic resolution is challenging. The other limitation in our case was the absence of *Vs* logs in the zones of interest. Only ~40 m length of Vs was acquired in well 32/2-1 within the deeper Brent Group and Lunde Formation. A machine learning model trained on a Central North Sea database (Rahman et al., 2020) was used to extract *Vs* employing Random Forest (RF), neural network (NN), and K-Nearest Neighbors (kNN) against the available *Vs* log depths. We compared the synthetic logs generated from the Greenberg and Castagna (1992) and machine learning methods with the acquired *Vs* log within the same zone (Fig. 18). On the *Lambda-Rho, Mu-Rho* plane (Goodway et al., 1997), the synthetic trend from Greenberg and Castagna (1992) drifts towards the quartz pole with an increase in Lambda-Rho compared to the acquired *Vs* that leans towards the carbonate pole. This has implications on lithology inversion from seismic, as minerals, especially carbonate would have lumped in the quartz domain. However, the thickness of carbonate stringers within our zone of study in the Smeaheia area is generally below seismic resolution that provides confidence in our inversion

results. It is evident here that the *Vs* generated using machine learning methods, particularly the neural network (NN) and K-Nearest Neighbors (kNN) yield better results compared to the Random Forest (RF) method. However, in our previous work (Rahman et al., 2020) the RF method showed better correlations within the Heather and Draupne Formation zones. Although in the present study, uncertainty related to the usage of right machine learning method exists, however, in other cases, the machine learning methods can be useful to generate synthetic *Vs* as input for seismic inversion.

Our proposed equation (Eq. (3)) for calculating shale volume is meant only for low TOC shales. The maximum TOC in Draupne Formation in well 32/4-1 is 3% (NPD, 2020) that yields reasonable results with Equation (3). High TOC contents tend to pull the data point towards "southwest" in an *AI, Vp/Vs* ratio plane, which in the presence of acquired *Vs* may require a different quantification approach. As the fluid and lithology extraction solutions are not unique, the rock physics-based deterministic methods have limitations. We are working to mitigate the data holes in extracted cubes (e.g., Fig. 16) and the inherent uncertainties, using a stochastic approach.

4. Conclusions

We found Sognefjord Formation the best candidate due to a sheet-like continuous deposition and optimum reservoir properties for CO_2 storage in the Smeaheia area, with carbonate-related permeability barriers considered helpful in the lateral distribution of injected CO_2. The Fensfjord Formation was identified as the second-best quality reservoir
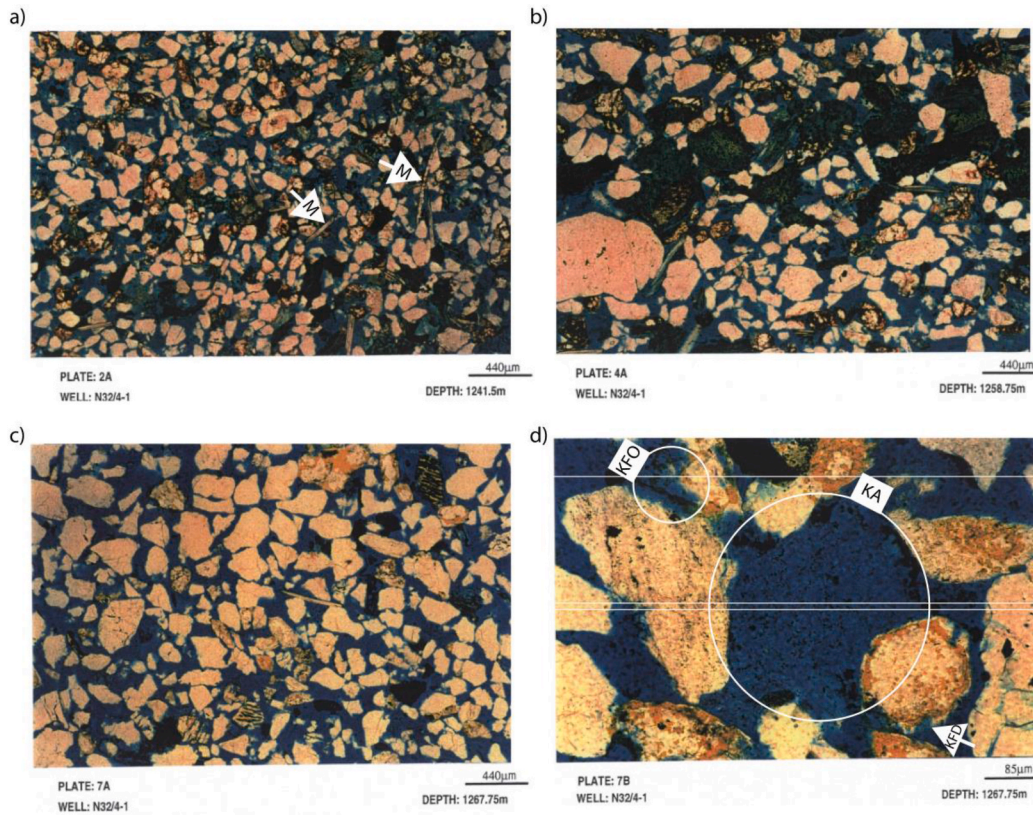
Fig. 17. Thin section images of sandstone at various depths (m MDRKB) of Sognefjord Formation core in well 32/4-1. (a) Intermediate permeability (~602mD) sandstone, (b) low permeability (70mD) sandstone, (c) high permeability (4600mD) sandstone. (d) A zoomed view of the high permeability sandstone (Modified after Martin and Lowrey, 1997). KA: Kaolinite, KFD: K-Feldspar Dissolution, KFO: K-Feldspar Overgrowth, and M: Muscovite.
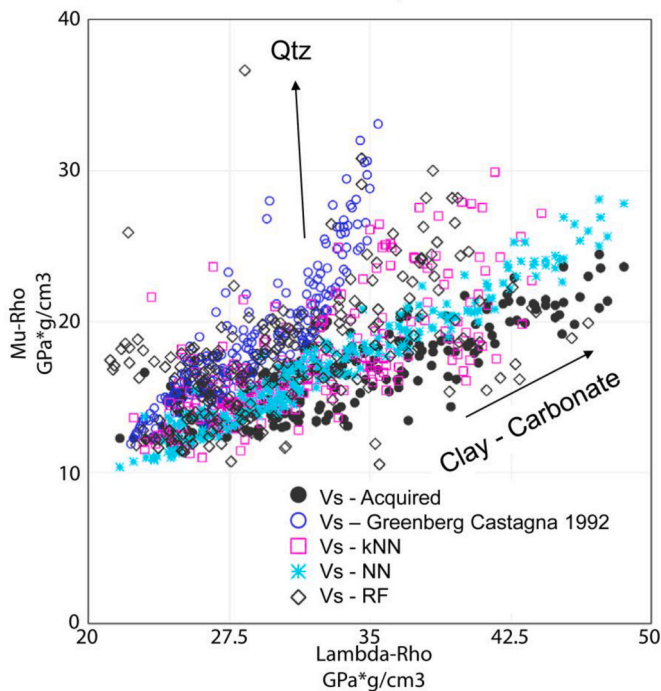

Fig. 18. Comparison of the acquired *Vs* with synthetic *Vs* generated using the Greenberg and Castagna (1992), and other selected machine learning methods, i.e., K-Nearest Neighbors (kNN), Neural Network (NN), and Random Forest (RF).

with the sand layers having suitable reservoir properties for CO_2 storage. The lower part of Fensfjord Formation comprises occasional deltaic sand deposition with possible lateral constrictions, which may pose a barrier for the injected CO_2.

A prograding shoreface possibly deposited the sands of Sognefjord, Fensfjord, and Krossfjord Formations. There is a prominent sheet-like sand distribution in the Sognefjord and Fensfjord Formations. The shoreface sand body also migrated along the strike towards the north gradually, from older Krossfjord to the younger Sognefjord Formations. The presence of various deltaic related sand bodies with uncertain lateral restrictions, low gross thickness, and moderate reservoir properties make the Krossfjord Formation the least suitable for CO_2 storage. For all the three sandstone formations (Sognefjord, Fensfjord, and Krossfjord), the porosity and permeability are increasing in the east towards the well 32/2-1 for always being present within the mechanically compacted zone.

We infer the uplift in the west (towards the well 32/4-1) to be approximately 1100 m, whereas the uplift is 1300 m in the east (towards well 32/2-1). At maximum burial depth, the reservoir sandstones have been exposed to a temperature higher than 70 °C in well 32/4-1. Therefore, the Sognefjord Formation in well 32/4-1 exhibits partial quartz cementation for being exposed to such temperature. The level of cementation increases in the deeper Fensfjord, and Krossfjord Formations, deteriorating the porosity.

The newly conceived equations for calculating V_{sh} and *Phi* from inverted seismic data yielded meaningful results despite the absence of acquired *Vs* logs. The resulted cubes were helpful in delineating the lateral changes in the reservoir sandstones; the vertical visibility was, however, dependent on the seismic resolution limitations.

Our study signifies the usage of nonlinear equations to calculate the reservoir properties from the inverted seismic readily; however, we

recommend future work on a similar line using a stochastic approach to take into account the inherent uncertainties of the input parameters.

CRediT author statement

Manzar Fawad: Conceptualization, Methodology, Formal analysis, Writing – original draft preparation. MD Jamilur Rahman: Data curation, Software, Validation, Writing- Reviewing,and Editing. Nazmul Haque Mondol: Project administration, Supervision, Validation, Writing- Reviewing, and Editing.

Declaration of competing interest

The authors declare the following financial interests/personal relationships which may be considered as potential competing interests: A patent applications "Rock physics model for shale volume estimation in subsurface reservoirs" was filed in Norwegian Industrial Property Office (NIPO), Ref no. AR412254832 on 23.01.2021. A Provisional patent application was also filed with the same title in the U.S. Patent and Trademark Office (USPTO), No. 63140896 on 24.01.2021.

Acknowledgments

References

Aki, K., Richards, P.G., 1980. Quantitative Seismology: Theory and Methods. Freeman.

Aksu, I., Bazilevskaya, E., Karpyn, Z.T., 2015. Swelling of clay minerals in unconsolidated porous media and its impact on permeability. GeoResJ 7, 1–13.

Aplin, A.C., Macquaker, J.H., 2011. Mudstone diversity: origin and implications for source, seal, and reservoir properties in petroleum systems. AAPG Bull. 95, 2031–2059.

Asquith, G.B., Krygowski, D., Gibson, C.R., 2004. Basic well log analysis. American Association of Petroleum Geologists Tulsa, vol. 16.

Avseth, P., Mukerji, T., Mavko, G., 2005. Quantitative Seismic Interpretation: Applying Rock Physics Tools to Reduce Interpretation Risk. Cambridge university press.

Avseth, P., Veggeland, T., 2015. Seismic screening of rock stiffness and fluid softening using rock-physics attributes. Interpretation 3. SAE85–SAE93.

Avseth, P., Veggeland, T., Horn, F., 2014. Seismic screening for hydrocarbon prospects using rock-physics attributes. Lead. Edge 33, 266–274.

Bernabé, Y., Fryer, D.T., Hayes, J.A., 1992. The effect of cement on the strength of granular rocks. Geophys. Res. Lett. 19, 1511–1514.

Bjørkum, P.A., Oelkers, E.H., Nadeau, P.H., Walderhaug, O., Murphy, W.M., 1998. Porosity prediction in quartzose sandstones as a function of time, temperature, depth, stylolite frequency, and hydrocarbon saturation. AAPG Bull. 82, 637–648.

Bjørlykke, K., Egeberg, P.K., 1993. Quartz cementation in sedimentary basins. AAPG Bull. 77, 1538–1548.

Bjørlykke, K., Jahren, J., 2015. Sandstones and sandstone reservoirs. In: Petroleum Geoscience. Springer, pp. 119–149.

Bosch, M., Mukerji, T., Gonzalez, E.F., 2010. Seismic inversion for reservoir properties combining statistical rock physics and geostatistics: a review. Geophysics 75, 75A165–75A176.

Brown, A.R., 2010. GC Dim Spots in Seismic Images as Hydrocarbon Indicators. Search and Discovery.

Buland, A., Omre, H., 2003. Bayesian linearized AVO inversion. Geophysics 68, 185–198.

Chadwick, R.A., Zweigel, P., Gregersen, U., Kirby, G.A., Holloway, S., Johannessen, P.N., 2004. Geological reservoir characterization of a CO2 storage site: the utsira sand, sleipner, northern North Sea. Energy 29, 1371–1381.

Chuhan, F.A., Kjeldstad, A., Bjørlykke, K., Høeg, K., 2003. Experimental compression of loose sands: relevance to porosity reduction during burial in sedimentary basins. Can. Geotech. J. 40, 995–1011.

Connolly, P., 1999. Elastic impedance. Lead. Edge 18, 438–452.

Dreyer, T., Whitaker, M., Dexter, J., Flesche, H., Larsen, E., 2005. From spit system to tide-dominated delta: integrated reservoir model of the Upper Jurassic Sognefjord Formation on the Troll West Field. In: Geological Society, London, Petroleum Geology Conference Series. Geological Society of London, pp. 423–448.

Dvorkin, J., Nur, A., 1996. Elasticity of high-porosity sandstones: theory for two North Sea data sets. Geophysics 61, 1363–1370.

Ehrenberg, S.N., 1993. Preservation of anomalously high porosity in deeply buried sandstones by grain-coating chlorite: examples from the Norwegian continental shelf. AAPG (Am. Assoc. Pet. Geol.) Bull. 77, 1260–1286.

Fatti, J.L., Smith, G.C., Vail, P.J., Strauss, P.J., Levitt, P.R., 1994. Detection of gas in sandstone reservoirs using AVO analysis: a 3-D seismic case history using the Geostack technique. Geophysics 59, 1362–1376.

Fawad, M., Hansen, J.A., Mondol, N.H., 2020. Seismic-fluid detection-a review. Earth Sci. Rev. 103347.

Fawad, M., Mondol, N.H., Jahren, J., Bjørlykke, K., 2011. Mechanical compaction and ultrasonic velocity of sands with different texture and mineralogical composition. Geophys. Prospect. 59, 697–720.

Fawad, M., Mondol, N.H., Jahren, J., Bjørlykke, K., 2010. Microfabric and rock properties of experimentally compressed silt-clay mixtures. Mar. Petrol. Geol. 27, 1698–1712.

Gardner, G.H.F., Gardner, L.W., Gregory, A.R., 1974. Formation velocity and density—the diagnostic basics for stratigraphic traps. Geophysics 39, 770–780.

Giles, M.R., 1997. Diagenesis: A Quantitative Perspective: Implications for Basin Modelling and Rock Property Prediction. Springer.

Goodway, B., Chen, T., Downton, J., 1997. Improved AVO fluid detection and lithology discrimination using Lamé petrophysical parameters;"λρ","μρ", & "λ/μ fluid stack", from P and S inversions. In: SEG Technical Program Expanded Abstracts 1997. Society of Exploration Geophysicists, pp. 183–186.

Greenberg, M.L., Castagna, J.P., 1992. Shear-wave velocity estimation in porous rocks: theoretical formulation, preliminary verification and applications. Geophys. Prospect. 40, 195–209.

Halland, E.K., Mujezinovic, J., Riis, F., Bjørnestad, A., Meling, I.M., Gjeldvik, I.T., Tappel, I.M., Bjørheim, M., RØD, R., PHAM, V., 2014. CO2 Storage Atlas: Norwegian Continental Shelf. Norwegian Petroleum Directorate.

Hampson, D.P., Russell, B.H., Bankhead, B., 2005. Simultaneous inversion of prestack seismic data. In: SEG Technical Program Expanded Abstracts 2005. Society of Exploration Geophysicists, pp. 1633–1637.

Hansen, J.A., Yenwongfai, H., Fawad, M., Mondol, N., 2017. Estimating exhumation using experimental compaction trends and rock physics relations, with continuation into analysis of source and reservoir rocks: Central North Sea, offshore Norway. In: SEG Technical Program Expanded Abstracts 2017. Society of Exploration Geophysicists, pp. 3971–3975.

Hart, B.S., Macquaker, J.H., Taylor, K.G., 2013. Mudstone ("shale") depositional and diagenetic processes: implications for seismic analyses of source-rock reservoirs. Interpretation 1. B7–B26.

Herwanger, J., Koutsabeloulis, N., 2011. Seismic geomechanics: how to build and calibrate geomechanical models using 3D and 4D seismic data. EAGE.

Holgate, N.E., Jackson, C.A., Hampson, G.J., Dreyer, T., 2015. Seismic stratigraphic analysis of the middle jurassic Krossfjord and Fensfjord formations, Troll oil and gas field, northern North Sea. Mar. Petrol. Geol. 68, 352–380.

Kemper, M., Gunning, J., 2014. Joint Impedance and Facies Inversion–Seismic Inversion Redefined. First Break 32.

Kinn, S., Foldøy, P., Pettersen, K., Ramstad, F., Rasmussen, H., Hansen, T.H., Goldsmith, P.J., 1997. Final Well Report 32/4-1. Phillips Petroleum Company Norway, NPD Factpages.

Lancaster, S., Whitcombe, D., 2000. Fast-track 'coloured' inversion. In: SEG Expanded Abstracts, pp. 1298–1301.

Lee, M.W., 2003. Velocity Ratio and its Application to Predicting Velocities. US Department of the Interior, US Geological Survey.

Lehocki, I., Avseth, P., Mondol, N.H., 2020. Seismic methods for fluid discrimination in areas with complex geologic history—A case example from the Barents Sea. Interpretation 8, SA35–SA47.

Lindseth, R.O., 1972. Approximation of acoustic logs from seismic traces. J. - Can. Well Logging Soc. 5, 13–26.

Luo, C., Ba, J., Carcione, J.M., Huang, G., Guo, Q., 2020. Joint PP and PS prestack seismic inversion for stratified models based on the propagator matrix forward engine. Surv. Geophys. 41, 987–1028.

Ma, X.-Q., 2001. Global joint inversion for the estimation of acoustic and shear impedances from AVO derived P-and S-wave reflectivity data. First Break 19, 557–566.

Marcussen, Ø., Maast, T.E., Mondol, N.H., Jahren, J., Bjørlykke, K., 2010. Changes in physical properties of a reservoir sandstone as a function of burial depth–The Etive Formation, northern North Sea. Mar. Petrol. Geol. 27, 1725–1735.

Martin, M.A., Lowrey, C.J., 1997. Sedimentology and Petrography of the Upper Jurassic Cored Interval from Well 32/4-1 (No. 7944/Id). Robertson Research International Limited.

Mavko, G., Mukerji, T., Dvorkin, J., 2009. The Rock Physics Handbook: Tools for Seismic Analysis of Porous Media. Cambridge University Press.

Mondol, N.H., Bjørlykke, K., Jahren, J., 2008a. Experimental compaction of kaolinite aggregates-effects of grain size on mudrock properties. In: 70th EAGE Conference and Exhibition Incorporating SPE EUROPEC 2008. European Association of Geoscientists & Engineers, p. 40.

Mondol, N.H., Bjørlykke, K., Jahren, J., Høeg, K., 2007. Experimental mechanical compaction of clay mineral aggregates—changes in physical properties of mudstones during burial. Mar. Petrol. Geol. 24, 289–311.

Mondol, N.H., Fawad, M., Jahren, J., Bjørlykke, K., 2008b. Synthetic mudstone compaction trends and their use in pore pressure prediction. First Break 26, 43–51.

Mulrooney, M.J., Osmond, J., Skurtveit, E., Wu, L., Braathen, A., 2018. Smeaheia, a potential northern North Sea CO2 storage site: structural description and de-risking

strategies. In: Fifth CO2 Geological Storage Workshop. European Association of Geoscientists & Engineers, pp. 1–5.

NPD, 2020. Norwegian Petroleum Directorate Fact-Pages. [WWW Document]. URL accessed 8.3.20. https://factpages.npd.no.

Ødegaard, E., Avseth, P., 2004. Well Log and Seismic Data Analysis Using Rock Physics Templates. First Break (October).

PetroWiki, 2021. Permeability Determination [WWW Document]. URL accessed 3.24.21. https://petrowiki.spe.org/Permeability_determination.

Rahman, M.J., Fawad, M., Mondol, N.H., 2020. Organic-rich shale caprock properties of potential CO2 storage sites in the northern North Sea, offshore Norway. Mar. Petrol. Geol. 122, 104665.

Riley, N., 2010. Geological storage of carbon dioxide. Issues Environ. Sci. Technol. 29, 155.

Schmitt, D.R., 2015. Geophysical properties of the near surface earth: seismic properties. In: Treatise on Geophysics. Elsevier, pp. 43–87.

Sheriff, R.E., Geldart, L.P., 1995. Exploration Seismology. Cambridge university press.

Shuey, R.T., 1985. A simplification of the Zoeppritz equations. Geophysics 50, 609–614.

Smith, G.C., Gidlow, P.M., 1987. Weighted stacking for rock property estimation and detection of gas. Geophys. Prospect. 35, 993–1014.

Statoil, A.S., 2016. Mulighetsstudie - Planlegging og prosjektering av et CO2-lager på norsk kontinentalsokkel (No. OED 15/1785. Undergrunnsrapport Smeaheia.

Sundal, A., Nystuen, J.P., Dypvik, H., Miri, R., Aagaard, P., 2013. Effects of geological heterogeneity on CO2 distribution and migration–a case study from the Johansen Formation, Norway. Energy Procedia 37, 5046–5054.

Sundal, A., Nystuen, J.P., Rørvik, K.-L., Dypvik, H., Aagaard, P., 2016. The lower jurassic johansen formation, northern North sea–depositional model and reservoir characterization for CO2 storage. Mar. Petrol. Geol. 77, 1376–1401.

Thyberg, B., Jahren, J., Winje, T., Bjørlykke, K., Faleide, J.I., 2009. From mud to shale: rock stiffening by micro-quartz cementation. First Break 27, 53–59.

Thyberg, B.I., Jordt, H., Bjørlykke, K., Faleide, J.I., 2000. Relationships between sequence stratigraphy, mineralogy and geochemistry in Cenozoic sediments of the northern North Sea. Geological Society, London, Special Publications 167, 245–272.

Timur, A., 1968. An investigation of permeability, porosity, and residual water saturation relationships. In: SPWLA 9th Annual Logging Symposium. Society of Petrophysicists and Well-Log Analysts.

Verm, R., Hilterman, F., 1995. Lithology color-coded seismic sections: the calibration of AVO crossplotting to rock properties. Lead. Edge 14, 847–853.

Whitcombe, D.N., Connolly, P.A., Reagan, R.L., Redshaw, T.C., 2002. Extended elastic impedance for fluid and lithology prediction. Geophysics 67, 63–67.

Yenwongfai, H., Mondol, N.H., Lecomte, I., Faleide, J.I., Leutscher, J., 2018. Integrating facies-based Bayesian inversion and supervised machine learning for petro-facies characterization in the Snadd Formation of the Goliat Field, south-western Barents Sea. Geophys. Prospect. 67, 1020–1039.

Yenwongfai, H.D., Mondol, N.H., Faleide, J.I., Lecomte, I., 2017. Prestack simultaneous inversion to predict lithology and pore fluid in the Realgrunnen Subgroup of the Goliat Field, southwestern Barents Sea. Interpretation 5, SE75–SE96.

Zhao, L., Geng, J., Cheng, J., Han, D., Guo, T., 2014. Probabilistic lithofacies prediction from prestack seismic data in a heterogeneous carbonate reservoir. Geophysics 79, M25–M34.

Zoeppritz, K., 1919. VII b. Über Reflexion und Durchgang seismischer Wellen durch Unstetigkeitsflächen. Nachrichten von der Gesellschaft der Wissenschaften zu Göttingen. Mathematisch-Physikalische Klasse 1919 66–84.